The Partitioning of Meridional Heat Transport from the Last Glacial Maximum to CO_2 Quadrupling in Coupled Climate Models

AARON DONOHOE

Polar Science Center, Applied Physics Laboratory, University of Washington, Seattle, Washington

KYLE C. ARMOUR

School of Oceanography and Department of Atmospheric Sciences, University of Washington, Seattle, Washington

GERARD H. ROE

Department of Earth and Space Sciences, University of Washington, Seattle, Washington

DAVID S. BATTISTI AND LILY HAHN

Department of Atmospheric Sciences, University of Washington, Seattle, Washington

(Manuscript received 22 October 2019, in final form 11 February 2020)

ABSTRACT

Meridional heat transport (MHT) is analyzed in ensembles of coupled climate models simulating climate states ranging from the Last Glacial Maximum (LGM) to quadrupled CO_2. MHT is partitioned here into atmospheric (AHT) and implied oceanic (OHT) heat transports. In turn, AHT is partitioned into dry and moist energy transport by the meridional overturning circulation (MOC), transient eddy energy transport (TE), and stationary eddy energy transport (SE) using only monthly averaged model output that is typically archived. In all climate models examined, the maximum total MHT (AHT + OHT) is nearly climate-state invariant, except for a modest (4%, 0.3 PW) enhancement of MHT in the Northern Hemisphere (NH) during the LGM. However, the partitioning of MHT depends markedly on the climate state, and the changes in partitioning differ considerably among different climate models. In response to CO_2 quadrupling, poleward implied OHT decreases, while AHT increases by a nearly compensating amount. The increase in annual-mean AHT is a smooth function of latitude but is due to a spatially inhomogeneous blend of changes in SE and TE that vary by season. During the LGM, the increase in wintertime SE transport in the NH midlatitudes exceeds the decrease in TE resulting in enhanced total AHT. Total AHT changes in the Southern Hemisphere (SH) are not significant. These results suggest that the net top-of-atmosphere radiative constraints on total MHT are relatively invariant to climate forcing due to nearly compensating changes in absorbed solar radiation and outgoing longwave radiation. However, the partitioning of MHT depends on detailed regional and seasonal factors.

1. Introduction

The total (ocean plus atmosphere) meridional heat transport (MHT) across a latitude circle by the coupled (ocean–atmosphere) climate system must, on long time scales, be balanced by the net top-of-atmosphere (TOA) radiative deficit spatially integrated over the polar cap bounded by a latitude circle (e.g., Vonder Haar and Oort 1973). This constraint offers two conceptually different but numerically equivalent frameworks for diagnosing and analyzing MHT. In a *dynamic* framework, MHT is equal to the vertically and zonally integrated net transport of energy across the latitude circle by atmospheric and oceanic motions due to the contrasts in energy content of equatorward and poleward flowing air/water (Lorenz 1953; Oort 1971). In an *energetic* framework, MHT is equal to the net TOA radiative deficit integrated over the extratropics or, equivalently, the net radiative excess integrated over the tropics. The hemispheric-scale radiative imbalance results from the equator-to-pole

Corresponding author: Aaron Donohoe, adonohoe@u.washington.edu

Publisher's Note: This article was revised on 21 April 2020 to replace Figs. 2 and 4–10, which were processed at a lower resolution when originally published.

DOI: 10.1175/JCLI-D-19-0797.1

gradient of absorbed solar radiation (ASR) being steeper than that of outgoing longwave radiation (OLR; Trenberth and Stepaniak 2004; Oort and Vonder Haar 1976).

In a seminal paper, Stone (1978) argued that the observed maximum poleward MHT in each hemisphere (MHT_{MAX}) is primarily dictated by Earth–sun geometry and relatively insensitive to the details of the atmospheric state due to nearly canceling contributions of the equator-to-pole gradient in planetary albedo and OLR. More recent work has demonstrated that the large-scale distribution of net TOA radiation can vary substantially between different climate models because cloud properties fundamentally control the ASR distribution (Donohoe and Battisti 2011) but have a modest impact on OLR. As a result, MHT_{MAX} differs by as much as 20% between different climate models in simulations of the preindustrial climate due to differences in cloud distributions/properties (Donohoe and Battisti 2012). However, several studies have demonstrated that *within a single model* MHT_{MAX} is nearly invariant to the state of the oceanic circulation (Farneti and Vallis 2013; Enderton and Marshall 2009), in the interannual variability (Vellinga and Wu 2008) and across paleoclimate states (Yang et al. 2015b). These results raise two key questions. First, how do MHT and its partitioning vary across climate states within ensembles of comprehensive, coupled global climate models (GCMs), given that clouds (and other forcings and feedbacks) can cause substantial changes in net TOA radiation? Second, what dynamical processes in the atmosphere and ocean contribute the MHT changes under climate forcing?

Here we consider MHT and its changes as simulated by an ensemble of comprehensive climate models participating in phase 5 of the Coupled Model Intercomparison Project (CMIP5; Taylor et al. 2012). We examine MHT within three different climate states: the climate at the Last Glacial Maximum (LGM), the climate under preindustrial (PI) conditions, and the climate with CO_2 levels set at 4 times the preindustrial concentration ($4 \times CO_2$). Earth's simulated global-mean surface temperature differs by approximately 10°C between the LGM simulations and the end of the 150-yr-long $4 \times CO_2$ simulations owing to the substantial increase in CO_2 and the elimination of large Northern Hemisphere ice sheets. Nonetheless, the ensemble-average MHT_{MAX} is nearly invariant between the simulated LGM, PI, and $4 \times CO_2$ climate states (Fig. 1a) changing by only 4% in the Northern Hemisphere (NH) and by only 2% in the Southern Hemisphere (SH). This result suggests that while cloud properties and their changes play an important role for the intermodel spread of MHT_{MAX} in climate models when forced by identical (preindustrial) forcings (Donohoe and Battisti 2012), the large-scale distribution of net TOA radiation, and thus MHT, is nearly invariant over a wide range of climate states (Fig. 1), just as Stone (1978) speculated.

The smooth, monotonic decrease in both (annual mean) ASR and OLR from the equator to pole mandates that MHT be a smooth and continuous function of latitude peaking in magnitude in the midlatitudes of each hemisphere (Trenberth and Stepaniak 2003b). Yet the atmospheric and oceanic circulations that accomplish the total MHT have a rich spatial structure (Trenberth and Caron 2001; Armour et al. 2019). In the deep tropics the atmosphere and ocean make comparable contributions to MHT (Fig. 2a), each dominated by the mass-overturning circulation in the atmospheric Hadley cells and wind-driven oceanic cells, respectively (Held 2001). In the extratropics (poleward of 30° latitude) the atmosphere does the lion's share of the MHT and is composed of the following transport processes: (i) transient eddies, which dominate energy transport in the midlatitude with latent- and sensible-heat transports that peak on the equatorward and poleward side of the storm track, respectively; (ii) stationary eddies in the subtropics associated with monsoons that transport latent heat during the summer in both hemispheres; and (iii) orographically and diabatically (i.e., land–ocean contrast) forced stationary eddies in the NH winter that transport sensible heat poleward on the poleward flank of the storm track (Fig. 3; Masuda 1988).

How do these different circulations adjust to produce a nearly invariant and meridionally smooth pattern of MHT across radically different climate states? Previous studies point to compensating changes in the various components that compose total MHT:

- *Oceanic and atmospheric energy transports*. If TOA radiation is climate-state invariant, changes in meridional (implied) oceanic heat transport (OHT) must be compensated by changes in meridional atmospheric heat transport (AHT), as originally proposed by Bjerknes (1964). This principle has been demonstrated using idealized models in which ocean basin geometry (Enderton and Marshall 2009) and the planetary rotation rates (Vallis and Farneti 2009) are changed; in both cases, distinct changes occurred in ocean circulations and OHT, but MHT (= OHT + AHT) remained nearly unchanged due to compensating AHT changes. In other modeling studies, the compensation between OHT and AHT is imperfect (i.e., MHT changes) due to large changes in sea ice cover (Enderton and Marshall 2009) or in cloud cover (X. Liu et al. 2018) such that changes in ASR are not balanced by those in OLR.
- *Oceanic and atmospheric energy transports*. In response to global warming, the moistening of the atmosphere results in an increase in moisture transport (Held and

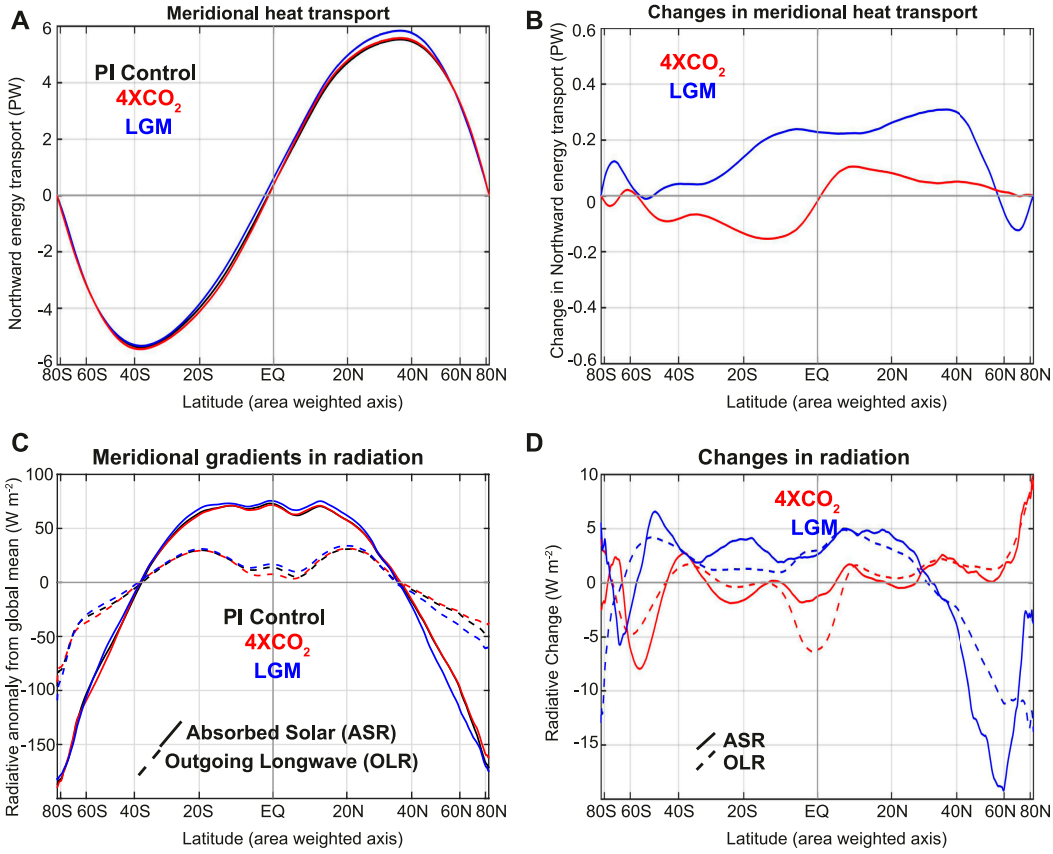

FIG. 1. (a) Ensemble-averaged total (ocean plus atmosphere) annual-mean meridional heat transport (MHT) in preindustrial (PI; black), abrupt carbon dioxide quadrupling (4 × CO_2; red), and Last Glacial Maximum (LGM; blue) CMIP5 simulations. Only the seven models that span all three simulations are included in the ensemble average. (b) The changes in MHT between the 4 × CO_2 and PI simulations (red), and between the LGM and PI simulations (blue). (c) Ensemble-averaged annual- and zonal-mean radiation in PI (black), 4 × CO_2 (red), and LGM (blue). Solid lines show the net solar radiation at TOA (absorbed solar radiation; ASR) and dashed lines show the outgoing longwave radiation (OLR). The global mean has been removed from ASR and OLR to emphasize the meridional gradients. (d) The changes in ASR (solid) and OLR (dashed), with global mean removed, between the 4 × CO_2 and PI simulations (red), and between the LGM and PI simulations (blue).

Soden 2006) in both the deep tropics (equatorward transport in the surface branch of the Hadley cell) and midlatitudes (poleward transient eddy transport). Climate models show that changes in latent heat transport are opposed by changes in sensible heat transport in both regions, resulting in a modest change in total AHT (Hwang and Frierson 2010; Armour et al. 2019).

- *Transient and stationary eddy transports in the atmosphere*. Model simulations suggest that in response to the enhanced topography of the Laurentide ice sheet during the LGM, AHT by atmospheric stationary eddies increases (Li and Battisti 2008), but transient eddy AHT simultaneously decreases, despite the enhanced meridional temperature gradient (Donohoe and Battisti 2009), leaving AHT and total MHT nearly unchanged.

Despite these compensation mechanisms, it is not clear why the equator-to-pole gradient in net TOA radiation is so constant as to produce nearly invariant MHT over a wide range of climates. Additionally, it is not clear why total MHT remains invariant when there are large changes in the mix of processes responsible for AHT (Trenberth and Stepaniak 2003a; Armour et al. 2019).

Traditionally, the partitioning of AHT requires that the transient eddy energy transport be calculated from high temporal resolution (i.e., six hourly) data—a computationally expensive calculation to perform across an ensemble of models. For this reason, the change in AHT partitioning under climate forcing has been diagnosed in single model studies (Wu et al. 2011; Enderton and Marshall 2009; Yang et al. 2015a) but not across a full ensemble of models. Changes in AHT due to increased CO_2 differ substantially across climate models due to the

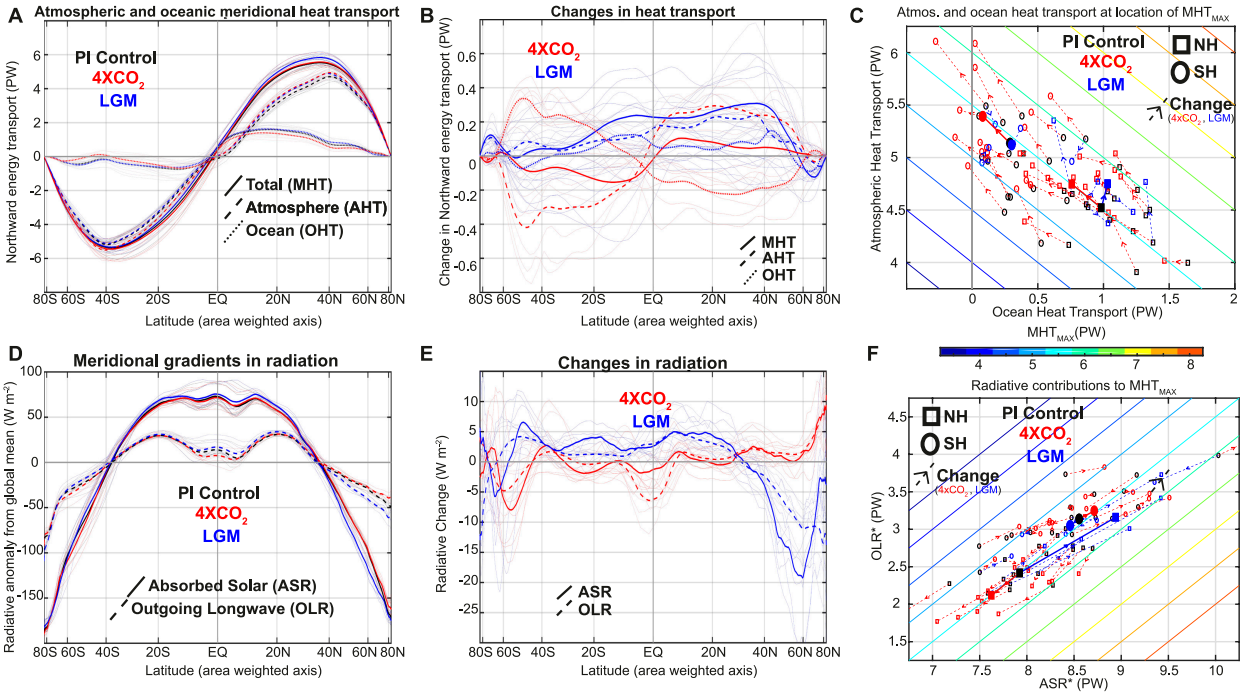

FIG. 2. (a) Annual-mean MHT (solid) partitioned between the atmosphere (AHT; dashed) and ocean (OHT; dotted) in PI (black), $4 \times CO_2$ (red), and LGM (blue) CMIP5 simulations. Thin lines show individual models and thick lines show the ensemble average. (b) The changes in MHT (solid), AHT (dashed), and OHT (dotted) between the $4 \times CO_2$ and PI simulations (red), and between the LGM and PI simulations (blue). (c) Scatterplot of OHT and AHT at the latitude where MHT achieves its maximum value (MHT_{MAX}) in each hemisphere. Squares show the NH and circles show the SH. Larger, filled markers represent the ensemble means. The dashed lines with arrows show the changes between the PI and $4 \times CO_2$ (red), and between the PI and LGM (blue) simulations, respectively, using the same model. Colored contours show lines of constant MHT_{MAX} with colors in the color bar below. (d) Annual and zonal-mean radiation in PI (black), $4 \times CO_2$ (red), and LGM (blue): ASR (solid) and OLR (dashed). The global mean has been removed from all fields to emphasize the meridional gradients. (e) Changes in ASR (solid) and OLR (dashed) between the $4 \times CO_2$ and PI simulations (red), and between the LGM and PI simulations (blue). (f) Scatterplot of contribution of ASR gradients (ASR*; abscissa) and OLR gradients (OLR*; ordinate) to MHT_{MAX}. Symbols, lines, and color bar are as in (c).

intermodel spread in the spatial structure of cloud feedbacks and ocean heat uptake (Trenberth and Fasullo 2010; Hwang and Frierson 2010; Hwang et al. 2011; Zelinka and Hartmann 2012; Frierson and Hwang 2012; Huang and Zhang 2014; Armour et al. 2019). Therefore, AHT changes identified within a single model might not isolate robust physical mechanisms from those contingent on the specific cloud parameterization within a single model.

The primary goal of this work is to partition the mean state and forced changes in MHT in ensembles of coupled GCMs in order to identify (i) model biases in the mix of processes contributing to total MHT and (ii) changes in the partitioning of MHT in response to climate forcing that are robust across the models. We describe a methodology that allows AHT to be partitioned into different circulations (overturning, stationary eddies, transient eddies) and thermodynamic (latent, sensible, potential) contributions from standard monthly mean climate model output. Conceptually similar methodologies have been used in single model studies (Hill et al. 2015; Xiang et al. 2018; Rencurrel and Rose 2018, 2020). Here, we apply this methodology across 20 different CMIP5 GCMs to consistently partitioning AHT and diagnose robust features and changes between LGM, preindustrial, and $4 \times CO_2$ climates.

This manuscript is organized as follows. In section 2a we discuss the calculation of MHT partitioning in the modern climate using satellite data and reanalysis products. In section 2b we introduce the methodology for partitioning AHT in climate models using monthly mean output, and in section 2c we demonstrate the accuracy of this method using high temporal output from a climate model. In section 3, we provide an overview of the results, focusing on the near invariance of total MHT from the LGM to $4 \times CO_2$ and how this result is achieved from dynamic and energetic perspectives. In section 4, we compare the MHT partitioning in climate models to the observational estimates. In sections 5 and 6,

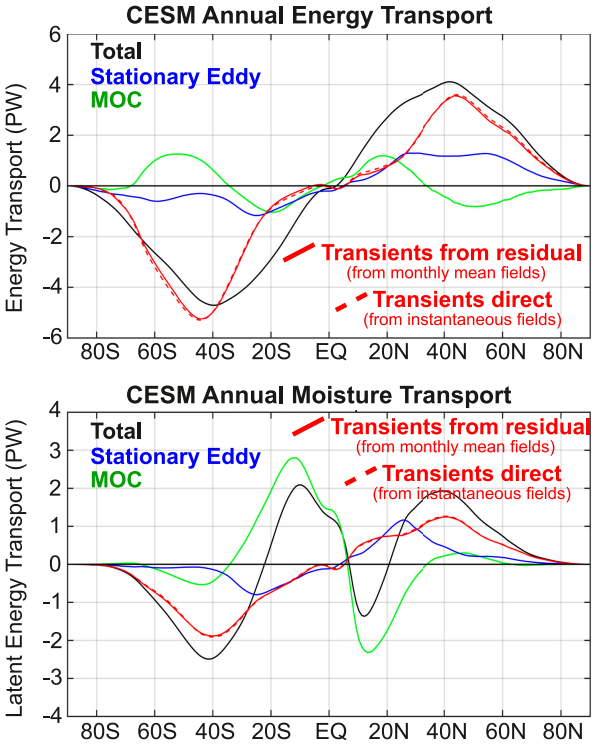

FIG. 3. Comparison of the zonally and vertically integrated transient eddy energy transport in CESM calculated using the residual method (section 2b; solid red lines) and the direct method (section 2a; dashed red lines). (top) The total annual-mean atmospheric energy transport. (bottom) The annual-mean atmospheric moisture transport.

we analyze the simulated MHT partitioning changes under 4 × CO_2 and LGM conditions, respectively. A summary and conclusions follow.

2. Data and methods

We partition MHT into OHT and AHT components, and further decompose AHT into contributions from the meridional overturning circulation (MOC), stationary eddies (SE), and transient eddies (TE):

$$\mathrm{MHT} = \mathrm{OHT} + \underbrace{\mathrm{MOC} + \mathrm{SE} + \mathrm{TE}}_{\mathrm{AHT}}. \qquad (1)$$

Our method partitions the MHT and the various components of AHT based on standard *monthly mean* climate model output, whereas the observed AHT is calculated directly from high temporal resolution three-dimensional atmospheric reanalysis products:

- *Observations*: We calculate the vertically and zonally integrated atmospheric energy transports (≡ AHT) from two different high temporal- (6-hourly) and spatial-resolution reanalysis products (see below) that permit an explicit calculation of the TE. Total MHT is calculated from satellite TOA radiation and the OHT is diagnosed as a residual as in Trenberth and Caron (2001).
- *Models:* We diagnose the total MHT from monthly mean TOA radiation, the implied OHT from the monthly mean surface energy fluxes, and AHT from the difference between TOA and surface energy fluxes. We then calculate the AHT associated with the time-invariant MOC and SE from monthly mean model output and diagnose the TE contribution as a residual.

The observational and model approaches differ because of the contrasting reliability and availability of model and observational data. Observationally based surface energy fluxes are not reliable at the global scale, whereas they are standard output from climate models. The direct calculation of three-dimensional TE that we use in the observations requires six-hourly atmospheric data that are readily available in reanalysis data but are not usually output in climate model simulations because of the enormous storage requirements. The details of these approaches are outlined below.

a. *Partitioning of MHT, AHT, and OHT in observations*

We begin by discussing the calculation of annual-mean oceanic and energy transports in an equilibrium climate state with no energy tendency (storage) in the atmosphere or ocean—thus providing the constraint of energy balance in the atmosphere and ocean. The total MHT at any latitude is equal to the energy transport required to balance the TOA radiative imbalance spatially integrated over the polar cap bounded by that latitude:

$$\mathrm{MHT}(\theta) = -2\pi a^2 \int_{\theta}^{90} \cos(\Theta)[\mathrm{ASR}(\Theta) - \mathrm{OLR}(\Theta)]\, d\Theta, \qquad (2)$$

where a is the radius of Earth, θ is latitude, and the cosine in the integrand accounts for spherical geometry. TOA radiation data is taken from the climatology of the Clouds and Earth's Radiant Energy Systems (CERES; Wielicki et al. 1996) Energy Balanced and Filled (EBAF) product (Loeb et al. 2009) version 4.0 from March 2000 to December 2016. In theory, global-mean energy balance ensures that MHT(θ) is independent of whether the TOA radiative imbalances are integrated from θ to the North Pole [as written in Eq. (2)] or from the South Pole to θ (with negative sign omitted). In practice, there is a nonzero global-mean value of ASR − OLR that must be subtracted from the integrand above to ensure

that MHT goes to zero at both poles; we assume this energy imbalance is spatially invariant and thus subtract a constant value at all latitudes, but note this as an important caveat to the calculation of climatological MHT in both observations and models. For the CERES EBAF data, the global radiative imbalance is equal to the long-term ocean heat uptake calculated from Argo data of $+0.65\,\mathrm{W\,m^{-2}}$ (Johnson et al. 2016). We use this same approach [i.e., Eq. (2)] to calculate MHT in coupled climate models where the ensemble-mean absolute values of global-mean TOA net radiative imbalance in PI models is $\approx 0.5\,\mathrm{W\,m^{-2}}$ (similar to that in CMIP3 models; Lucarini and Ragone 2011), which translates to a $\pm$ 0.1-PW adjustment of $\mathrm{MHT_{MAX}}$. Energy imbalance in the PI control simulations could arise from either not reaching full equilibration or from a lack of energy conservation, primarily within the atmospheric model component (Hobbs et al. 2016). Because energy nonconservation appears to be largely invariant over time and across forcing scenarios of CMIP5 models (Hobbs et al. 2016), we expect the calculation of heat transport changes to be largely unaffected by this issue.

We calculate the AHT as the vertically (mass weighted) and zonally integrated meridional transport of moist static energy (MSE) $= c_pT + Lq + gZ$, where T is the atmospheric temperature, c_p is the specific heat of air at constant pressure, L is the latent heat of vaporization of water, q is the specific humidity, g is the acceleration of gravity, and Z is the geopotential height. We use two different atmospheric reanalyses products for our calculations: (i) the NCEP reanalysis product (Kalnay et al. 1996), which has a horizontal spectral resolution of T62 and 17 vertical levels; and (ii) the ERA-Interim reanalysis product (Dee et al. 2011), which has a horizontal resolution of 1.5° and 37 vertical levels. We use 6-hourly fields to calculate the energy transport for each month over the 2000–16 time period, averaging the results over all years to define the climatological AHT (for each month). The velocities and MSE are subdivided into the zonal and time mean, transient eddy, and stationary eddy components (as in Priestley 1948; Lorenz 1953). In this framework, the vertically and zonally integrated total energy transport is

$$\mathrm{AHT}(\theta) = \frac{2\pi a\cos(\theta)}{g}\int_0^{P_s} \underbrace{[\overline{V}][\overline{\mathrm{MSE}}]}_{\mathrm{MOC}} + \underbrace{[V^*\mathrm{MSE}^*]}_{\mathrm{SE}} + \underbrace{\overbrace{[V'^*\mathrm{MSE}'^*]}^{\mathrm{TE}} + \overbrace{[V]'[\mathrm{MSE}]'}^{\mathrm{TOC}}}_{\mathrm{Transients}} dp, \qquad (3)$$

where V is the meridional velocity and the vertical integral is over pressure p from the TOA to the surface, square brackets [] denote zonal averages, overbars $\overline{()}$ denote time averages over each month of analysis, asterisks (*) are departures from the zonal average, and primes ($'$) are departures from the time average. The calculation is performed at each latitude θ. The first term is the product of the time and zonal-mean meridional velocity and MSE and represents the MOC by way of the vertical gradient in MSE. We account for conservation of mass in the MOC energy transport by removing the vertically averaged MSE (Marshall et al. 2014) as opposed to using a barotropic wind correction (Trenberth and Stepaniak 2003a) because the resultant MOC has been shown to be more physically relevant on monthly time scales (Liang et al. 2018). The second term is the SE, which is poleward when the time-average eddy (i.e., monthly mean, anomaly from zonal mean) poleward velocity occurs in a warm (or wet) sector. The first two terms can be calculated from monthly mean data.

The third term is the TE due to the temporal covariance of V and MSE that is primarily associated with baroclinic synoptic eddies. The fourth term is the energy transport associated with the covariance of the zonal-mean overturning circulation and the vertical stratification that has previously been referred to as the transient overturning circulation (TOC; Marshall et al. 2014); it is two orders of magnitude smaller than the MOC in the deep tropics and two orders of magnitudes smaller than the eddy terms in the midlatitudes. Thus, herein we will ignore the TOC in our discussion of AHT and refer to the sum of the TOC and transient eddy energy transport simply as TE although we note that the term "transients" would be a more technically accurate word choice. The moist and dry components of AHT, SE, MOC, and TE are calculated from Eq. (3) by replacing the total MSE with the moist (Lq) and dry ($c_pT + gZ$) components, respectively.

OHT is calculated as the residual of the MHT determined from TOA radiation via Eq. (2) and the AHT calculated from the atmospheric reanalysis via Eq. (3) as in Trenberth and Caron (2001). Stated otherwise, the satellite-derived TOA radiation and reanalysis-derived AHT convergence constrains the surface energy fluxes (as a residual) at each latitude via the atmospheric energy balance. The oceanic energy balance requires that the surface heat fluxes are balanced by the ocean heat transport divergence and, thus, the implied $\mathrm{OHT}(\theta)$ is the spatial integral from the pole to θ.

b. *Partitioning of MHT and AHT using monthly average coupled climate model output*

We partition AHT in the CMIP5 models using monthly mean data because the six-hourly output needed to calculate the transient eddy energy transport in Eq. (3) is not

readily available for all models. However, the implied OHT at each latitude can be calculated accurately from the surface heat flux (SHF), which is composed from standard model output. The OHT is the spatial integral of the SHF over the polar cap bounded by that latitude:

$$\mathrm{OHT}(\theta) = -2\pi a^2 \int_{\theta}^{90} \cos(\Theta)[\mathrm{SHF}(\Theta)]\, d\Theta, \qquad (4)$$

a statement that (in equilibrium) the surface heat flux out of the ocean, beyond a latitude circle, is balanced by poleward ocean energy transport into the region. SHF is the net (radiative plus turbulent) *downward* energy flux at the surface:

$$\mathrm{SHF} = \underbrace{\mathrm{SW}\downarrow - \mathrm{SW}\uparrow + \mathrm{LW}\downarrow - \mathrm{LW}\uparrow}_{\text{Surface radiation}} - \underbrace{\mathrm{sensible}\uparrow - \mathrm{latent}\uparrow}_{\text{Turbulent}}, \qquad (5)$$

where SW and LW refer to the shortwave and longwave radiative fluxes with arrows denoting downwelling and upwelling radiation at the surface. We note that Eq. (4) is valid when the ocean is in *equilibrium*. When the system is not in equilibrium (i.e., the ocean is accumulating energy), Eq. (4) expresses the *implied* OHT, which is the sum of OHT and the spatial integral of the tendency in ocean heat content. Thus, our comparison of OHT diagnosed from Eq. (4) in the PI and LGM (equilibrium) simulations versus the $4 \times CO_2$ (transient) simulations does *not* constrain changes in OHT since the latter includes the impact of transient ocean storage. However, the change in AHT that accompanies changes in implied OHT is independent of whether the implied OHT change results from lateral ocean energy transport or transient ocean heat content changes since the atmosphere only responds to the associated SHF.

Total MHT is calculated as in the observations from the net TOA radiation via Eq. (2). AHT is then constrained by Eq. (1) as the residual of MHT and OHT calculated from TOA radiation and SHFs, respectively. Stated otherwise, the difference between TOA radiation and the (downward) SHF constrains the net (radiative plus diabatic) heating of a column of atmosphere that can be spatially integrated to calculate AHT. As in the observations, the AHT by the SE and MOC is calculated from the monthly mean fields of V and MSE via Eq. (3). The energy transport by transients (TE + TOC) is calculated as the residual of the atmospheric energy transport by the stationary circulation (SE + MOC) and the total AHT. As noted in our discussion of the observed AHT partitioning, TOC is much smaller than TE, and we herein refer to the energy transport by the transients (calculated as a residual in the models) as TE for simplicity even though the TOC is also included in the calculation.

We next describe how to calculate the moist and dry components of AHT from monthly mean model output. The latent heat transport at any given latitude [$\mathrm{AHT}_{\mathrm{moist}}(\theta)$] equals the integral of evaporation E minus precipitation P, poleward of that latitude, multiplied by the latent heat of vaporization L:

$$\mathrm{AHT}_{\mathrm{moist}}(\theta) = -2\pi a^2 \int_{\theta}^{90} \cos(\Theta)\{L[E(\Theta) - P(\Theta)]\}\, d\Theta. \qquad (6)$$

The dry contribution to total AHT can then be calculated from the residual of total AHT and $\mathrm{AHT}_{\mathrm{moist}}$. The moist and dry transport in the SE and MOC is calculated in the same manner as the observations, by replacing MSE in Eq. (3) with the moist (Lq) and dry ($c_pT + gZ$) components. $\mathrm{TE}_{\mathrm{moist}}$ is calculated as the residual of the total $\mathrm{AHT}_{\mathrm{moist}}$ in Eq. (6) minus the sum of the latent heat transport by the steady atmospheric circulations ($\mathrm{SE}_{\mathrm{moist}}$ and $\mathrm{MOC}_{\mathrm{moist}}$):

$$\mathrm{TE}_{\mathrm{moist}} = \mathrm{AHT}_{\mathrm{moist}} - (\mathrm{SE}_{\mathrm{moist}} + \mathrm{MOC}_{\mathrm{moist}}). \qquad (7)$$

$\mathrm{TE}_{\mathrm{dry}}$ is the difference between the total TE and $\mathrm{TE}_{\mathrm{moist}}$.

The above discussion pertains to the calculation of annual-mean AHT and OHT where (in an equilibrium climate) ocean and atmospheric energy content changes are negligible. On seasonal time scales, we must account for the tendency in atmospheric energy content in our calculation of AHT and seasonal storage of energy in the ocean in the interpretation of implied OHT. The implementation of these considerations is discussed in detail in the appendix.

c. *Validation of partitioning technique*

The AHT partitioning method used on climate models uses monthly averaged model output and relies on the closure of the atmospheric energy budget to diagnose the transient eddy energy transport as the residual of that demanded by TOA radiation and surface fluxes minus the energy transport by the stationary circulation. Here, we analyze the closure of the atmospheric energy budget in a single climate model using high-frequency atmospheric fields alongside climatological energy fluxes at the TOA and surface as a validation of the accuracy of the methods based on monthly mean fields proposed above.

We run a 10-yr PI simulation using the NCAR CESM coupled model and output the time-averaged product

of instantaneous (i.e., at each dynamic time step) V and T ($\overline{VT}$), V and Q ($\overline{VQ}$), and V and Z ($\overline{VZ}$) as a three-dimensional field (pressure level, latitude, longitude). The output is interpolated to pressure levels from the model's native vertical coordinate akin to the CMIP archived data. This choice was made to test if the interpolation to pressure levels introduces energy budget residuals. The transient MSE transport ($\mathrm{TE}_{\mathrm{direct}}$) is calculated as the difference between the time-averaged products minus the product of the time-average fields:

$$\mathrm{TE}_{\mathrm{direct}} = \frac{2\pi a \cos(\theta)}{g}\int_0^{P_s} c_p(\overline{VT} - \overline{V}\,\overline{T}) + L(\overline{VQ} - \overline{V}\,\overline{Q}) + g(\overline{VZ} - \overline{V}\,\overline{Z})\,dp. \quad (8)$$

There is excellent agreement between TE energy transport calculated from the residual of total AHT and the stationary energy transport (solid red line in top panel Fig. 3) and the direct calculation of TE energy transport from the high-frequency fields via Eq. (8) (dashed red line). Similarly, $\mathrm{TE}_{\mathrm{moist}}$ calculated from the monthly mean fields via Eq. (7) (solid red line in bottom panel Fig. 3) is in excellent agreement with that calculated by Eq. (8) (dashed red line). These statements are equivalent to the statement that the energy and moisture budgets of the atmosphere in CESM are both closed. These results suggest that the residual method used in this manuscript accurately diagnoses the TE energy and moisture transport.

d. Climate model experiments analyzed

We analyze MHT partitioning in three different experiments performed as part of the CMIP5 suite of experiments: (i) PI control simulations run to equilibrium; (ii) abrupt carbon dioxide quadrupling ($4 \times CO_2$) from the PI base state; and (iii) LGM simulations forced by reduced greenhouse gas concentrations, prescribed ice sheet topography, and orbital parameters from 21 000 years ago (Braconnot et al. 2007a). We analyze all model simulations that are publicly available and that report all (monthly mean) output fields required for our analysis: precipitation, TOA radiation, radiative and turbulent energy fluxes at the surface, and three-dimensional atmospheric winds, temperature, geopotential height, and specific humidity. In total, output from 20 different models are included in the PI and $4 \times CO_2$ analyses, and 7 different models are included in the LGM analyses. PI and LGM climatologies are calculated from the last 50 years of the simulations; climatologies for the $4 \times CO_2$ simulations are calculated using years 50–100 after quadrupling.

3. Near invariance of total meridional heat transport from the LGM to $4 \times CO_2$

We now provide an overview of the MHT changes over the ensemble of climate simulations spanning the LGM to $4 \times CO_2$ as viewed from dynamic and energetic perspectives. We consider transport changes to be robust when the ensemble-mean change exceeds two standard deviations of the mean change.[1] This criterion roughly corresponds to a 95% confidence interval of ensemble-mean changes in a two-tailed t test.

In the ensemble average, total MHT in the LGM and $4 \times CO_2$ simulations is nearly identical to that in the PI simulations: the CMIP5 ensemble-average change in MHT is not significantly different from zero at all latitudes in the $4 \times CO_2$ simulations and outside of the NH midlatitudes in the LGM (Fig. 1b). However, while the total ensemble-mean MHT is climate-state invariant (excluding the LGM changes in the NH) the component contributions to MHT vary substantially and robustly across simulations. Compensating changes are seen in the broadest sense—from a dynamics perspective (in the partitioning of MHT between AHT and OHT) and from an energetic perspective (in the changes in the equator-to-pole gradient of OLR and ASR). The changes in $\mathrm{MHT}_{\mathrm{MAX}}$ in each model under $4 \times CO_2$ and LGM forcing are shown in Tables 1 and 2, respectively. $\mathrm{MHT}_{\mathrm{MAX}}$ changes within a single model can depart from the ensemble-mean change by as much as 0.3 PW in both hemispheres due to intermodel differences in the (spatial structure of) cloud radiative feedbacks (see Fig. 6d of Zelinka and Hartmann 2012).

From a dynamics perspective there is a robust increase in poleward AHT under $4 \times CO_2$ (Fig. 2b) in both hemispheres (Hwang and Frierson 2010) with nearly compensating decreases in implied poleward OHT (see Fig. 11B in Held and Soden 2006). The changes in implied OHT are due to the spatial pattern of transient ocean heat uptake that preferentially occurs in the high-latitude oceans (Marshall et al. 2015; Armour et al. 2016). It is unclear whether the increase in poleward AHT and decrease in implied OHT under $4 \times CO_2$ would also be a feature of the fully equilibrated $4 \times CO_2$ climate (Chengfei et al. 2019). We can visualize the degree of compensation between AHT and OHT changes by coplotting the magnitude of AHT and OHT at the latitude of maximum MHT (Fig. 2c) in both the NH (squares) and SH (circles); in this space, lines of constant

[1] The standard deviation of the mean change is the standard deviation of the change across models divided by the square root of the number of models.

TABLE 1. MHT_{MAX} in each model's PI simulation and its change under 4 × CO_2 forcing (PW).

	Northern Hemisphere		Southern Hemisphere	
	PI MHT_{MAX}	ΔMHT_{MAX}	PI MHT_{MAX}	ΔMHT_{MAX}
ACCESS1.0	5.28	0.00	4.75	−0.10
BCC_CSM1.1	5.69	+0.05	5.27	+0.06
CanESM2	5.46	+0.13	5.55	−0.14
NCAR CCSM4	5.57	−0.06	5.32	+0.20
CNRM CM5	5.41	−0.03	5.01	−0.12
CSIRO Mk5	5.16	+0.33	4.71	−0.29
FGOALS-s2	5.52	−0.11	5.45	+0.09
GISS-E2-R	5.21	+0.11	4.89	−0.05
GFDL CM3	6.03	−0.15	5.57	−0.31
GFDL-ESM2G	5.86	+0.11	4.89	−0.26
GFDL ESM2M	5.77	+0.15	4.91	−0.21
INM-CM4	5.38	−0.02	5.17	−0.02
IPSL-CM5A	5.42	−0.08	6.04	−0.14
IPSL-CM5B	5.42	+0.14	5.89	+0.00
MIROC5	4.90	+0.10	4.72	−0.16
MIROC-ESM	5.41	−0.15	5.59	+0.24
MPI-ESM-P	5.97	−0.13	5.77	−0.30
MPI-ESM-LR	5.90	+0.23	5.78	+0.31
MRI-CGCM3	5.76	0.00	5.08	+0.02
NorESM1	5.63	−0.15	5.31	+0.09
Ensemble mean	5.54	+0.03	5.26	+0.07

MHT_{MAX} have slope of −1 and are shown by the colored contour lines. Changes in AHT and OHT (denoted by dashed lines and arrows) under 4 × CO_2 (red) relative to the PI are primarily along lines of constant MHT_{MAX} in both the ensemble average and in individual models indicating near-perfect compensation between AHT and OHT. AHT and OHT changes in the LGM simulations (blue lines and arrows in Fig. 2c) also compensate for each other, but the compensation is not perfect as indicated by the drift of the blue lines across lines of constant MHT_{MAX}. MHT_{MAX} increases robustly in the NH under LGM forcing and thus the ensemble-mean increase in poleward AHT in the NH is unaccompanied by compensating OHT changes.

From an energetic perspective, the MHT can only change if the equator-to-pole gradient of net radiation at the TOA changes. In all three sets of simulations, the broadscale structure of ASR and OLR are nearly unchanged (cf. the red and blue lines in Fig. 1d) suggesting that the magnitude of MHT is constrained by Earth–sun geometry to zeroth order in accordance with Stone (1978). Furthermore, changes in the equator-to-pole gradient of ASR and OLR nearly compensate for each other (Figs. 1d and 2e). For example, in response to 4 × CO_2, extratropical ASR and OLR both increase (relative to their global-mean values) as the high-latitude surface albedo decreases (Donohoe and Battisti 2011) and polar amplification (e.g., Holland and Bitz 2003) enhances OLR via the Planck feedback leaving the net TOA radiative deficit over the extratropics nearly unchanged.

Donohoe and Battisti (2012) introduced a metric to formalize this radiative compensation over the polar cap bounded by the latitude (θ_{MAX}) where MHT = MHT_{MAX}

TABLE 2. MHT_{MAX} in each model's PI simulation and its change under LGM forcing (PW).

	Northern Hemisphere		Southern Hemisphere	
	PI MHT_{MAX}	ΔMHT_{MAX}	PI MHT_{MAX}	ΔMHT_{MAX}
MRI-CGCM3	5.76	0.00	5.08	−0.14
NCAR CCSM4	5.57	+0.48	5.32	−0.30
CNRM CM5	5.41	0.00	5.01	+0.06
IPSL-CM5-LR	5.11	+0.30	6.06	+0.27
MIROC-ESM	5.41	+0.57	5.59	+0.10
MPI-ESM-P	5.97	+0.27	5.77	+0.22
GISS-E2-R	5.21	+0.46	4.89	+0.07
Ensemble mean	5.49	+0.30	5.39	+0.04

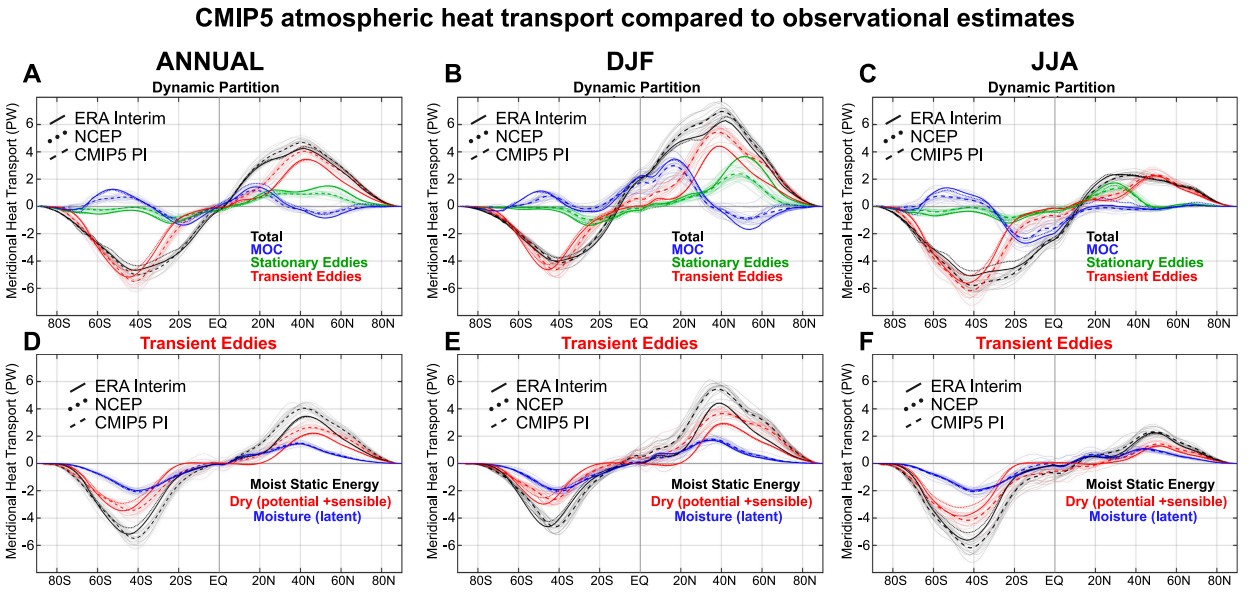

FIG. 4. (top) Atmospheric meridional heat transport calculated from atmospheric reanalysis (solid line, ERA; dotted line, NCEP) and CMIP5 PI simulations (dashed) with thin lines representing individual models and thick lines showing the ensemble average. The total moist static energy transport is partitioned into component circulation contributions: meridional overturning circulation (MOC; blue), stationary eddies (green), and transient (red). (bottom) The transient contribution to meridional energy transport decomposed into moist (latent; blue) and dry (potential + sensible; red) contributions. (a),(d) The annual mean, (b),(e) DJF, and (c),(f) JJA.

in each hemisphere. Let ASR* be the spatial integral of the deficit of ASR (relative to the global mean) poleward of θ_{MAX} and OLR* be the deficit of OLR over the same region, then $MHT_{MAX} = ASR^* - OLR^*$. Figure 2f shows that ASR* and OLR* each change by an order of 1 PW in response to LGM and 4 × CO_2 forcing with the most notable change being the robust increase of both quantities by more than 1 PW in the NH in the LGM simulations (blue squares). However, the changes in ASR* and OLR* mostly compensate for one another (the changes denoted by the lines with arrows are almost parallel to the contour lines of constant MHT_{MAX}) and, thus, MHT_{MAX} is nearly climate-state invariant despite large changes in the individual radiative components that constrain MHT. The only significant (ensemble mean) change in MHT_{MAX} occurs in the NH under LGM conditions where the increase in ASR* exceeds that in OLR* (the solid blue line connecting squares has slope less than 1 in Fig. 1f). Interestingly, the net TOA radiation during the LGM changes substantially regionally with decreases of ≈60 W m^{-2} over the Laurentide ice sheet (not shown) and zonal means decreases of ≈10 W m^{-2} (cf. the dashed and solid blue lines in Fig. 1d near 60°N) due to reduced ASR over the bright surface. However, there is a compensating increase in *net* TOA radiation poleward of 70°N due to decreased OLR associated with surface cooling that results in a near cancellation of OLR* and ASR*. These results show that despite large regional-scale net radiative changes, the equator-to-pole-scale net TOA radiation, and thus MHT_{MAX}, is approximately invariant across vastly different climate states.

We have seen that MHT_{MAX} is nearly climate-state invariant because there is near compensation from both dynamical and energetic perspectives. From a dynamics perspective, AHT and OHT changes nearly compensate. From an energetic perspective, ASR* and OLR* changes nearly compensate. We now look at a more detailed view of AHT changes partitioned into dynamic circulation changes and thermodynamic energy components.

4. Partitioning of heat transport: Comparison of models and observations

We begin with a brief comparison between models and observations of the dynamic (TE, SE, MOC) and thermodynamic (moist, dry) AHT partitioning, in both the annual mean and the solstitial season DJF and JJA (Fig. 4). We note at the onset that the comparison between PI simulations and the observed climate system over the 2000–16 time period is not an apples-to-apples comparison since the PI simulations represent an equilibrium climate state, whereas the observed system is in transient adjustment to anthropogenic forcing. Comparison between PI and historical simulations find

generally small (magnitudes less than 0.1 PW) differences in MHT and its partitioning between AHT and OHT. However, in all models the implied OHT in the Southern Hemisphere is approximately 0.1 PW smaller over the 2000–16 time period in the historical run as compared to that in preindustrial simulation in the same model while AHT is larger by approximately the same amount. We speculate that this results from transient ocean heat uptake in the Southern Ocean in response to historical anthropogenic forcing and this would bias the observed OHT low relative to the PI simulations should the same process be occurring in nature. The annual-mean AHT at the latitude of maximum poleward transport (AHT_{MAX}) in CMIP5 PI control simulations generally exceeds the observationally based estimates; AHT_{MAX} exceeds the ERA reanalysis calculation in 19 (out of 20) models in the NH and in 17 models in the SH. Similarly, AHT_{MAX} exceeds the NCEP reanalysis calculation in 17 models in the NH and in all models in the SH. This is primarily due to greater poleward TE during the winter season (red lines in Figs. 4b,c) and secondarily due to less equatorward energy transport in the Ferrel cell (midlatitude MOC) in the models compared to the observational estimate (primarily in the winter). This is somewhat of a puzzle because the strength of the Ferrel cell is generally thought to be a direct consequence of TE energy transport (Peixoto and Oort 1992). Interestingly, the annual-mean SE energy transport in models is biased low relative to the observations throughout the NH, a result that is remarkably consistent between the different reanalysis products. This model bias stems from too weak transport of sensible energy during the boreal winter (cf. the dashed and solid green lines in Fig. 4b) and too weak moisture transport in the monsoonal systems during the boreal summer (Fig. 4c).

In the tropics, energy transport by the MOC varies substantially between CMIP5 models and the ensemble average is biased low compared to the observations (Figs. 4a–c) in both the NH (by 17% and 29% of the ERA and NCEP values, respectively) and SH (by 27% and 14% of the ERA and NCEP values, respectively). This bias results from too little transport into the subtropics of the winter hemisphere at the latitude of maximum MOC (about 20°N in boreal winter and 20°S in austral winter; Figs. 4b,c). In the deep tropics (near the equator) the TE is in the same sense as the MOC but it is much stronger in the models than in the observations; TE is 40% of the MOC transport near the equator in the models. In contrast, transport by TE is negligible near the equator in both observational datasets (Donohoe et al. 2013). This model–observational mismatch is entirely due to dry TE (cf. the dashed and solid red lines in Figs. 4e,f).

The appendix (Fig. A1) shows a comparison of annual-mean MHT partitioned into AHT and implied OHT in models and observations where the observational estimates of OHT are calculated from the difference of the CERES-derived MHT and the NCEP/ERA-reanalysis-derived AHT. Observational MHT is within the model spread of MHT in both hemispheres. However, in general, models have stronger-than-observed poleward AHT and weaker-than-observed poleward OHT especially in the SH. Because our observed OHT is derived from the residual of MHT and AHT and has no direct observational constraint, we are reluctant to speculate on the dynamical cause of this apparent model bias.

The reader may be concerned that the model–observation mismatches highlighted above result from the different methodologies used to partition AHT in models and observations. There are two possible sources of methodological differences: 1) any sub-six-hourly covariances will not be accounted for in the observational TE potentially leading to a low bias, and 2) any nonenergy conserving process in the models (e.g., Lucarini and Ragone 2011) may lead to inconsistencies between the MHT diagnosed from energetic requirements versus those from dynamic processes biasing the TE transport calculated as a residual in unknown ways. However, we note that biases in MOC and SE are comparable in magnitude to those in TE and the former two contributions are calculated in exactly the same way in models and observations. This suggest that there are genuine, large differences in the partitioning of MHT between CMIP models and observations.

5. Energy transport partitioning changes under $4 \times CO_2$

Here we focus on the dynamic and thermodynamic contributions to the increase in poleward AHT under $4 \times CO_2$. In Figs. 5–7 we present the PI and $4 \times CO_2$ analyses for the annual mean, DJF, and JJA, respectively. Each figure shows the MOC, SE, and TE contributions to AHT, and each contribution is in turn split into its dry and moist components. The left-hand panels show the two climatologies, and the right-hand panels show the differences. Each of the 20 ensemble members is plotted, together with the ensemble mean. In what follows, we highlight several specific aspects of the analyses that we have found noteworthy. For those interested in exploring specific questions, the heat transport partitioning for all model are available in the online repository (https://atmos.uw.edu/~aaron/cmip_AHT_partition/).

The annual-mean total poleward AHT increases in both hemispheres under $4 \times CO_2$ and the change in AHT is a smooth function of latitude (Fig. 5b). However, the changes in the dynamical components of AHT have a rich meridional structure. Some of the component changes

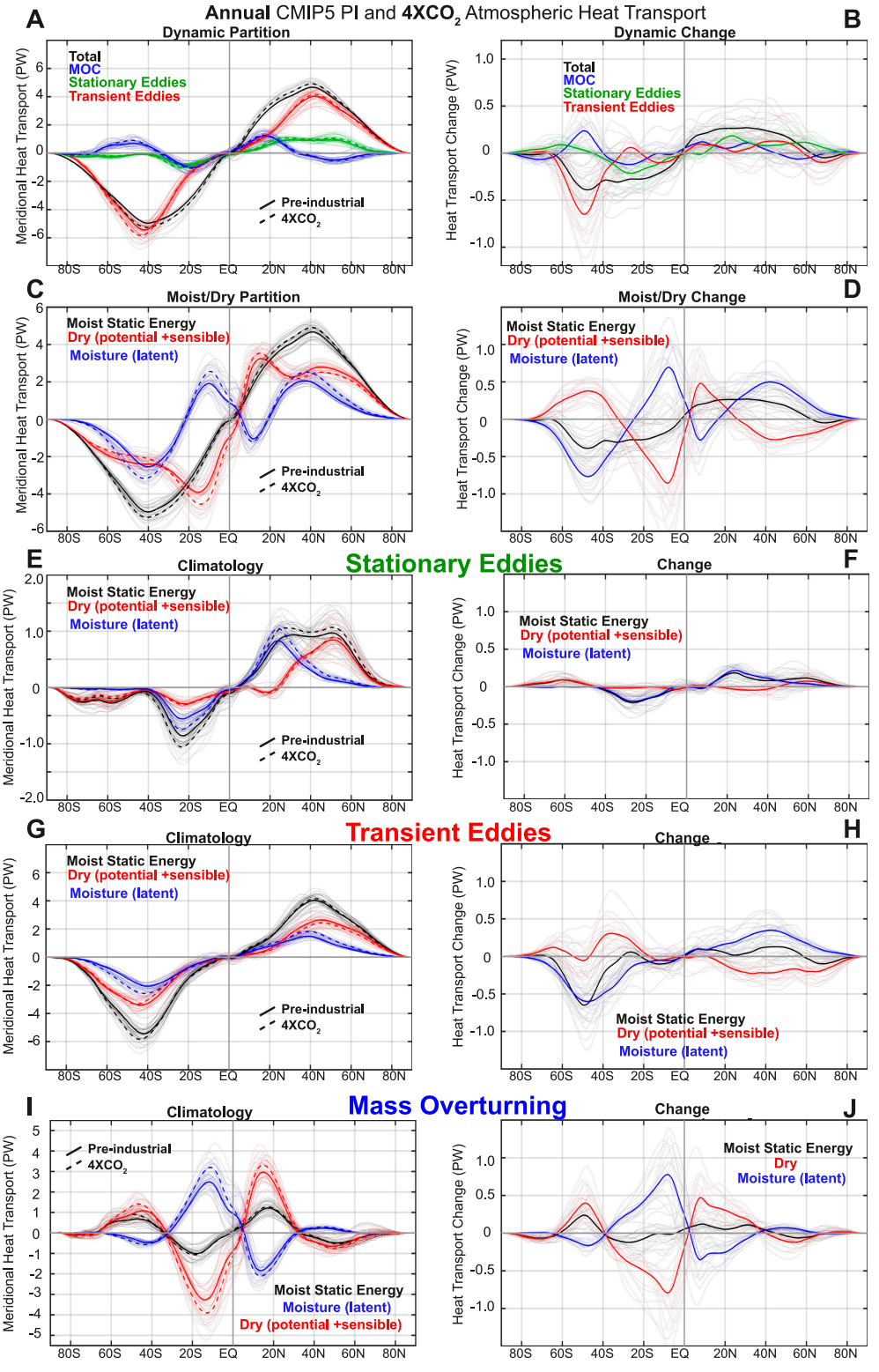

FIG. 5. (left) Annual-mean atmospheric energy transport in CMIP5 PI (solid lines) and 4 × CO_2 (dashed lines) simulations and (right) the changes between 4 × CO_2 and PI. (a),(b) The partitioning of energy transport into atmospheric circulations type: MOC (blue), stationary eddies (green), and transient eddies (red) with total shown in black. (c),(d) The partitioning of energy transport by energy type: dry (potential plus sensible; red) and moist (latent; blue). The moist and dry contributions within each circulation type: (e),(f) stationary eddies, (g),(h) transient eddies, and (i),(j) MOC. Note that the range on the *y* axis differs between the left-hand panels, and all the right-hand panels have the same range on the *y* axis.

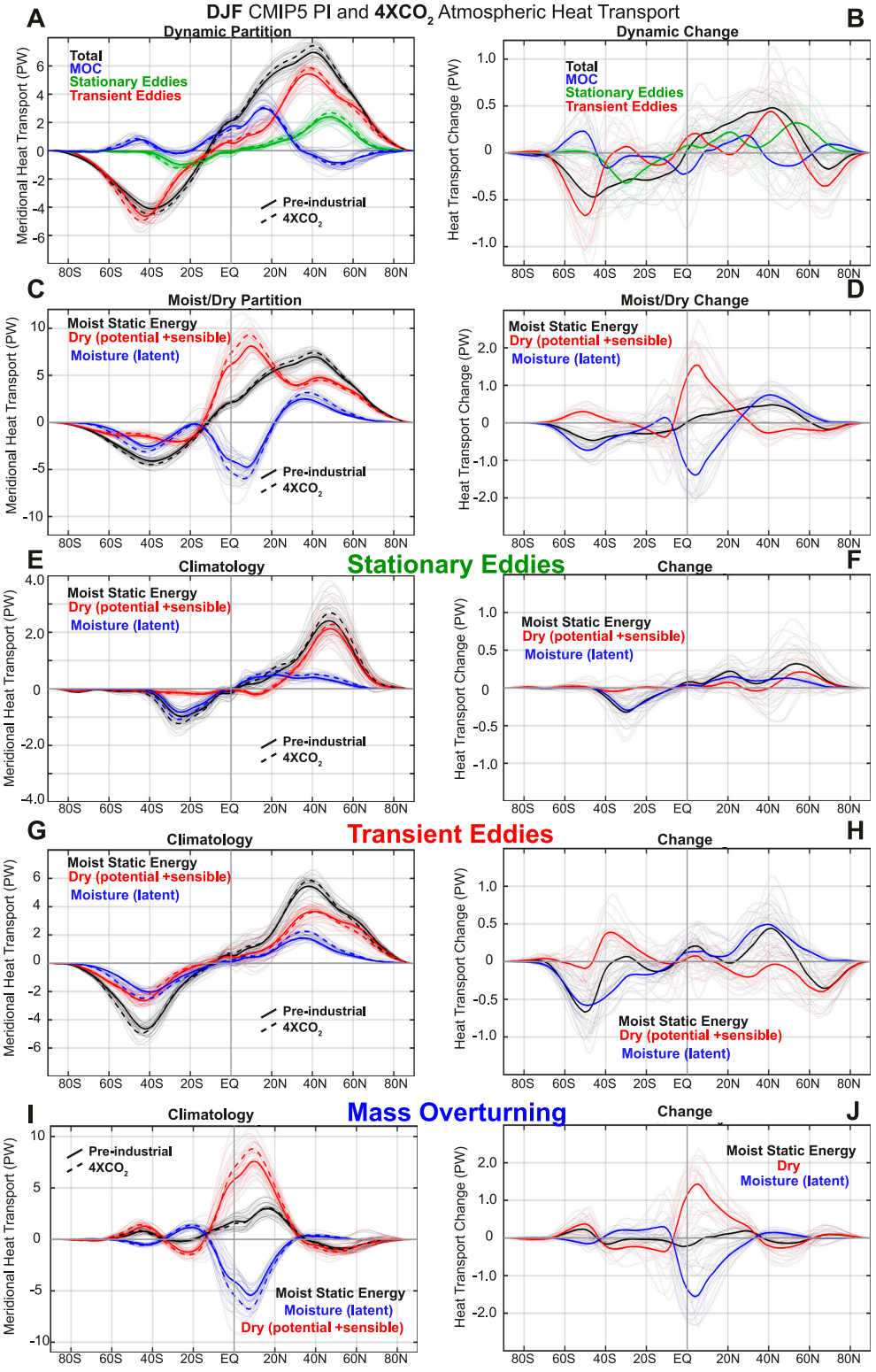

FIG. 6. As in Fig. 5, but for December–February (DJF). Note that the range on the *y* axis has been doubled relative to Fig. 5 in the moist/dry partitioning in (c) and (d), the MOC transport in (i) and (j), and the climatological stationary eddy transport in (e).

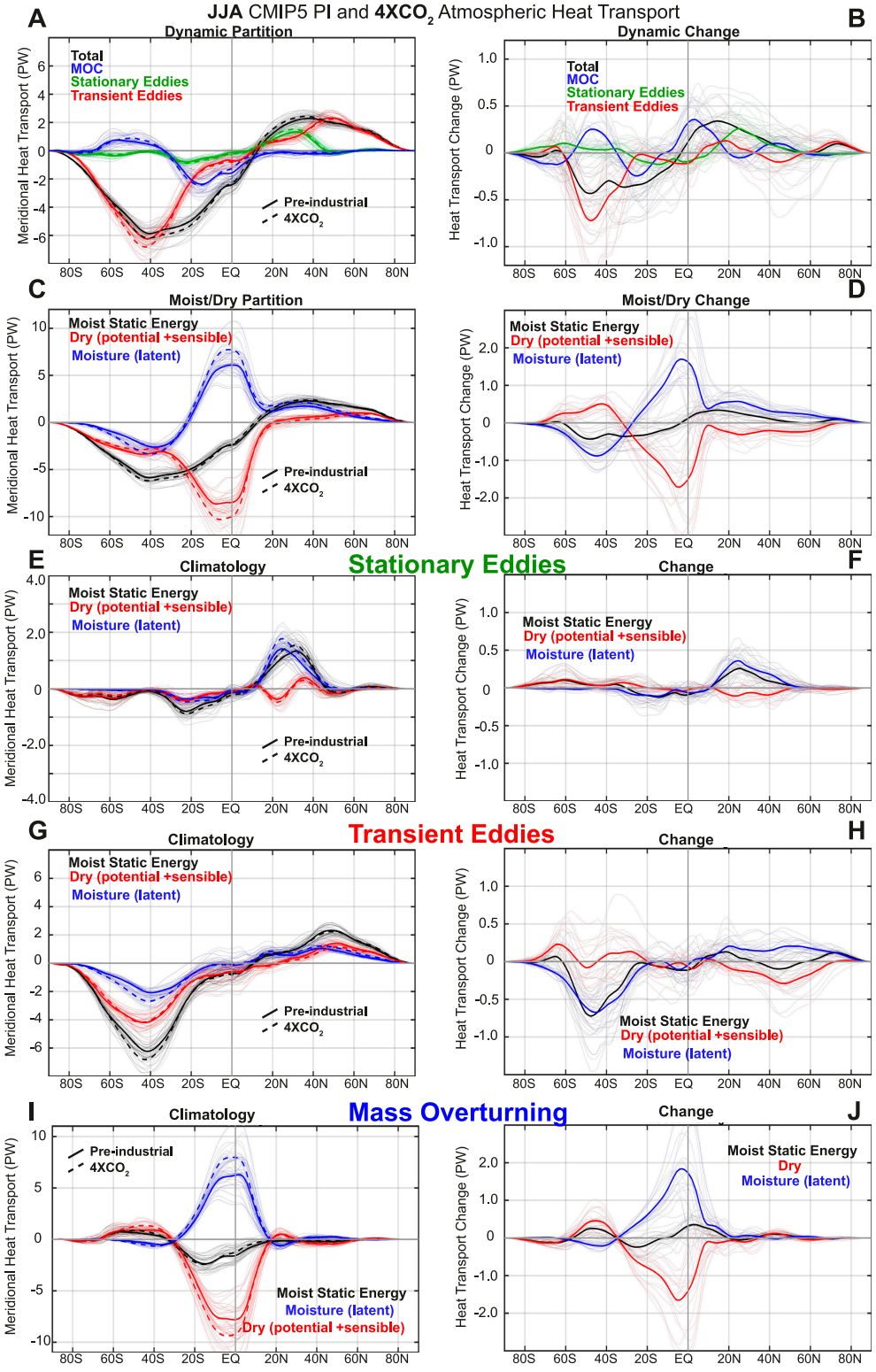

FIG. 7. As in Fig. 5, but for June–August (JJA).

are robust across the ensemble members, whereas others vary in sign and magnitude across the ensemble. Notably, for each model the component changes sum to a smooth increase in total poleward AHT (Figs. 5b,d).

The robust changes in AHT partitioning under $4 \times CO_2$ are as follows:

- An increase in poleward heat transport by TE in the SH storm-track regions (30°–60°S). This occurs during winter and summer (Figs. 6h and 7h). The ensemble-mean increases are due entirely to a robust increase in TE moisture transport. Changes in TE dry transport are ambiguous with nearly an equal number of models simulating increases and decreases. There is a robust compensating increase in the equatorward energy transport in the thermally indirect Ferrel cell as would be expected from the robust increase in low-level eddy heat flux convergence on the poleward flank of the storm track, forcing ascent. The meridional temperature gradient increases slightly in this region (not shown) during all seasons due to delayed Southern Ocean warming. As a result, the meridional moisture gradient increases owing to nearly constant relative humidity and the nonlinearity in the Clausius–Clapeyron equation. We speculate this strengthened meridional moisture gradient causes the enhanced poleward TE moisture transport.
- An increase in poleward moisture transport by stationary eddies in the subtropics of both hemispheres (10°–40°S and 10°–50°N) during summer (Figs. 6f and 7f). In the climatology, stationary waves associated with monsoon systems (Hurley and Boos 2015) are responsible for the maximum in moisture transport by stationary eddies that peaks near 25° latitude in the summer hemisphere. The increased moisture transport by stationary eddies in the $4 \times CO_2$ ensemble represents an intensification of these climatological transports (Figs. 6f and 7f) that are likely due to an increase in ambient atmospheric moisture (Hori and Ueda 2006).
- Large, nearly compensating changes in tropical moist and dry energy transport. In the PI climatology, the meridional overturning circulation transports moisture (≈4 PW of latent energy) into the summer hemisphere in the lower branch of the Hadley cell and dry energy (≈6 PW of sensible + potential) out of the summer hemisphere in the upper branch of the Hadley cell with a net energy transport (≈2 PW) away from the summer hemisphere. Under $4 \times CO_2$, the moistening of the surface and upward extension of the Hadley circulation as the tropopause rises results in an enhancement of the dry and moist energy transport in the MOC (Figs. 5j, 6j, and 7j) with small net changes (Held and Soden 2006; Yang and Dai 2015).
- Increases in poleward SE in the Southern Ocean (≈60°S). These changes are most prevalent during JJA and are entirely due to changes in sensible energy transport (Fig. 7e).

There are several changes in AHT that differ markedly among ensemble members. Most notably, the changes SE and TE in the NH midlatitudes during DJF (Figs. 6f,h). At 45°N during DJF, the poleward SE increases by 0.2 ± 0.7 PW and the poleward TE increases by +0.4 ± 0.6 PW, where the stated ± values are 2σ across the 20 ensemble members. The intermodel spread in TE and SE changes are strongly ($R = -0.71$) negatively correlated, resulting in a total AHT change of 0.6 ± 0.3 PW. This result suggests that the change in total AHT is more tightly constrained (by TOA radiation and SHF constraints) than the response of the individual circulation components. This implies a mechanism of compensation between the SE and TE changes.

The total midlatitude TE change is a tug-of-war between moist and dry components (Fig. 5h). The poleward latent energy transport increases in all models (mean = 0.4 PW) and the dry TE transport decreases (mean = −0.1 PW) in the majority of models but with remarkable spread (0.6 PW). In the midlatitudes in all seasons, intermodel differences in dry TE tend to reduce the intermodel spread of total AHT changes and make the resultant total AHT changes a smoother function of latitude.

TE contributes more to cross-equatorial AHT during the solstice seasons under $4 \times CO_2$ (Figs. 6a and 7a). As discussed in section 4, TE near the equator is larger in CMIP5 PI than in observational estimates. Under $4 \times CO_2$ the MOC still accomplishes the majority of AHT but the amplitude of the TE during the solstitial seasons is approximately 60% of MOC. In DJF, the changes in TE near the equator under $4 \times CO_2$ are comparable in magnitude to the change in MOC (Fig. 6b). This result raises concerns with attributing ITCZ shifts to changes in cross-equatorial AHT demanded by the hemispheric-scale energetics, which assume the tropical AHT changes are due to MOC changes (Schneider et al. 2014; Donohoe et al. 2013).

6. Energy transport partitioning changes under Last Glacial Maximum conditions

CMIP5 models robustly and unanimously simulate an increase in MHT in the NH in their LGM simulations (Fig. 8b; ensemble mean = +0.3 PW) primarily due to increases in AHT (mean = +0.2 PW). AHT increases in five of the seven models and decreases in the two models that have substantial increases in poleward OHT (Fig. 2b).

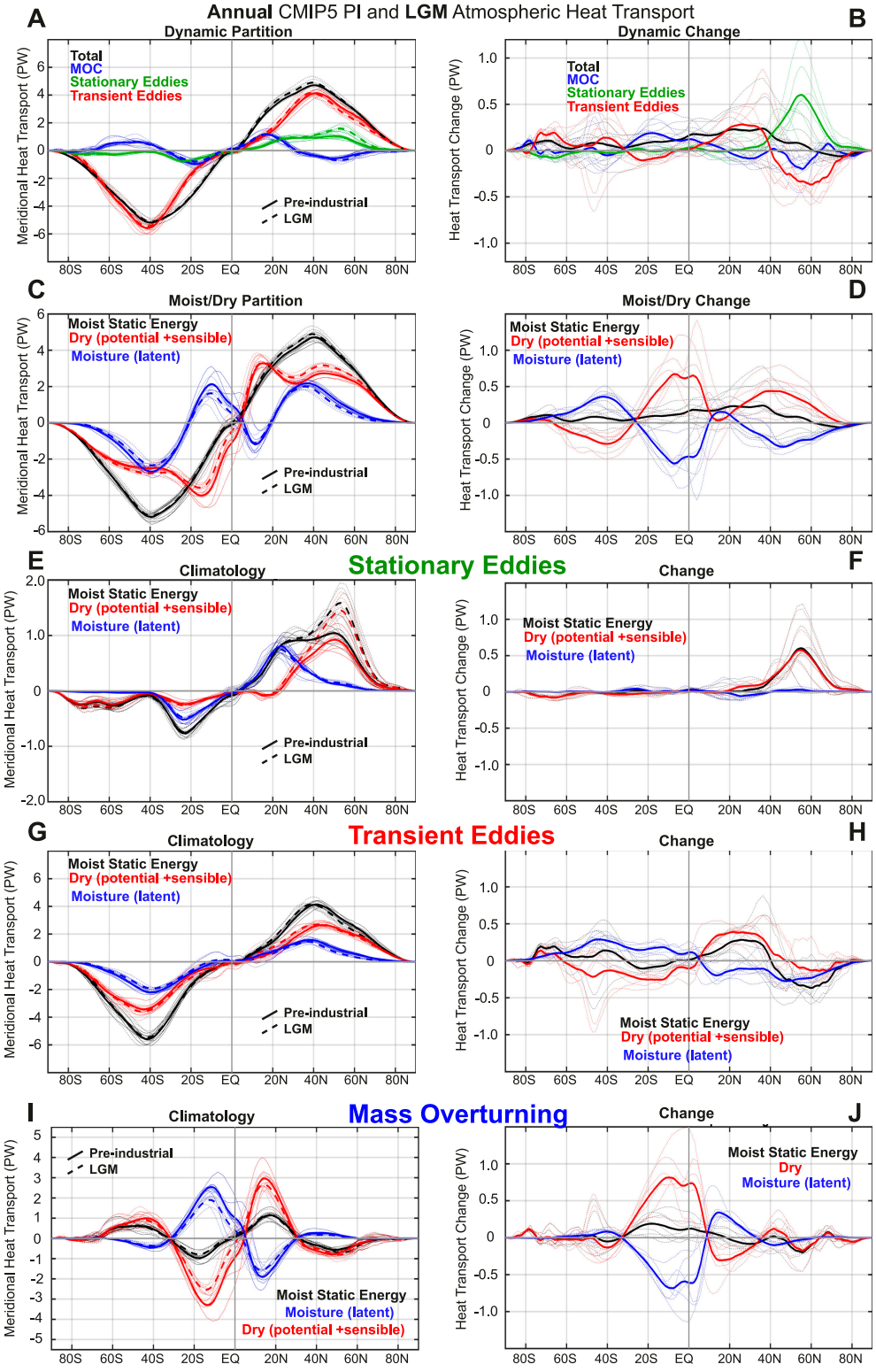

FIG. 8. As in Fig. 5, but for (left) PI (solid) and LGM (dashed) and (right) LGM-PI changes.

In contrast, changes in MHT and AHT in the SH are close to zero in the ensemble average (Figs. 8a,b). The most striking change during the LGM is the (≈+0.7 PW) enhancement of the NH SE around 55°N during DJF (Fig. 9f) that is seen in all models and in the ensemble mean; it is associated with the atmospheric stationary wave that is generated by the Laurentide ice sheet (e.g., Li and Battisti 2008) and transports sensible heat poleward (Fig. 9f) in the mid- and upper troposphere (not shown). In DJF, the increase in SE is compensated by a (≈−0.7 PW) decrease in TE that is displaced slightly equatorward of the SE change (Fig. 9b). The TE decrease is due to decreases in the poleward transport of both dry and moist energy (Fig. 9h). While a decrease in moisture transport by transient eddies is expected in a colder climate, the simultaneous decrease in dry TE is counterintuitive in a climate with an enhanced equator-to-pole temperature gradient, where one might expect stronger storm tracks based on baroclinic instability (Eady 1949). However, eddy kinetic energy has been shown to decrease in most LGM simulations because the stationary wave generated by the Laurentide ice sheet reduces the upper-level seeding of storms in the Atlantic domain (Donohoe and Battisti 2009). In the net, the DJF AHT in the NH is nearly unchanged during the LGM due to the compensation between SE and TE changes.

Interestingly, the ensemble-mean increase in AHT in the NH midlatitudes during the boreal *summer* is primarily a result of enhanced poleward TE centered around 40°N (ensemble-average change = 0.7 PW; Fig. 10f) combined with smaller magnitude increase in SE centered around 50°N (ensemble-average change = 0.3 PW; Fig. 10h).

In the SH, the total AHT and its partitioning is relatively unchanged in the LGM simulations (Figs. 8a,b). The only significant change is a decrease in poleward moist TE that compensates for the increase in poleward dry TE that is most prevalent in the austral winter (Fig. 10h). The total TE change is not significantly different from zero. Moist–dry compensation of energy transport changes is also seen in the MOC. In JJA, the cross-equatorial moist MOC into the NH decreases under LGM conditions with a nearly compensating decrease in dry MOC into the SH (Figs. 10i,j). Interestingly, the moist and dry changes in MOC transport during DJF are not simply a scalar change in the climatological transports (with the same underlying latitudinal structure); there is a southward shift of the distribution during the LGM that is most evident in DJF (Figs. 9i,j) due to a southward Hadley cell (and ITCZ) shift.

7. Summary and conclusions

Despite the large intermodel spread in climatological MHT in CMIP5 preindustrial simulations, the ensemble-mean MHT is in close agreement with the MHT observed in the NH (Donohoe and Battisti 2012) and biased low on average in the SH (Trenberth and Fasullo 2010) with the intermodel spread spanning the observational value. However, the partitioning of MHT in models is somewhat different from the partitioning in observations: (i) SH OHT is too weak in all climate models (Fig. A1), (ii) NH midlatitude TE is larger in climate models than that observed, and (iii) SE is weaker in the models than in observations especially in boreal winter (Fig. 4). Additionally, in the deep tropics, TEs provide a modest contribution to AHT in climate models, whereas AHT is almost entirely by the MOC in the observations. Remarkably, the intermodel spread in total MHT poleward of 50° in both hemispheres is small compared with the enormous spread in the component contributions (SE and TE), suggesting that relative weighting of the different transport processes is less constrained than is their net impact on the net TOA radiation. Furthermore, the large intermodel spread in MHT is primarily accomplished by intermodel differences in the TE sensible energy transport.

Total poleward meridional heat transport (MHT) is nearly invariant in an ensemble of models spanning from the LGM to the PI to a world with CO_2 quadrupled above PI levels; for example, the mean absolute magnitude of MHT change is 0.3 (0.1) PW and 0.2 (0.1) PW in the NH and SH, respectively, in response to LGM ($4 \times CO_2$) forcing. However, the partitioning of MHT between AHT and implied OHT and between the various atmospheric circulations (SE, TE, and MOC) and energetic (moist and dry) contributions changes substantially with climate forcing. Some of the changes in MHT partitioning are robust across the ensemble of climate models including the following: (i) TE latent heat transport increases in a warmer/moister world with nearly compensating decreases in TE sensible heat transport; (ii) the Hadley cell exports more sensible energy from the tropics to the subtropics in a warmer climate and imports more moisture into the tropics in the lower branch of the Hadley circulation; (iii) subtropical stationary waves associated with summer monsoons transport more moisture in a warmer world due to enhanced ambient humidity; (iv) implied OHT decreases under $4 \times CO_2$ (due to high-latitude ocean heat uptake) with a nearly compensating increase in AHT in both hemispheres; and (v) in response to LGM topography (e.g., the Laurentide ice sheet), NH stationary eddy sensible heat transport increases during the boreal winter. Other changes in the partitioning of MHT vary substantially between climate models including the net (moist plus dry) change in transient eddy energy transport with warming and the change in midlatitude stationary eddy

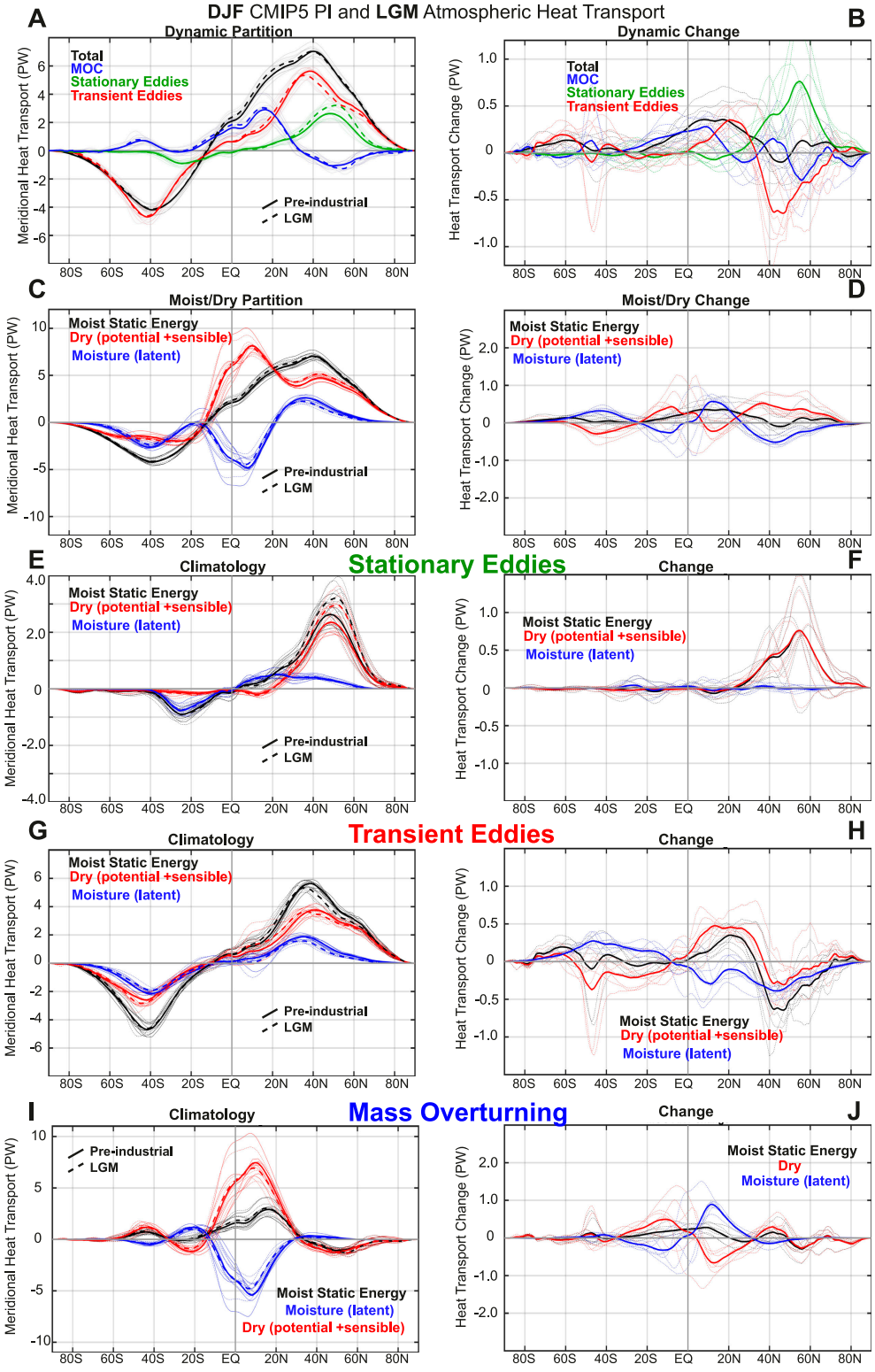

FIG. 9. As in Fig. 8, but for DJF. Note that the range on the *y* axis has been doubled relative to Fig. 8 in the moist/dry partitioning in (c) and (d), the MOC transport in (i) and (j), and the climatological stationary eddy transport in (e).

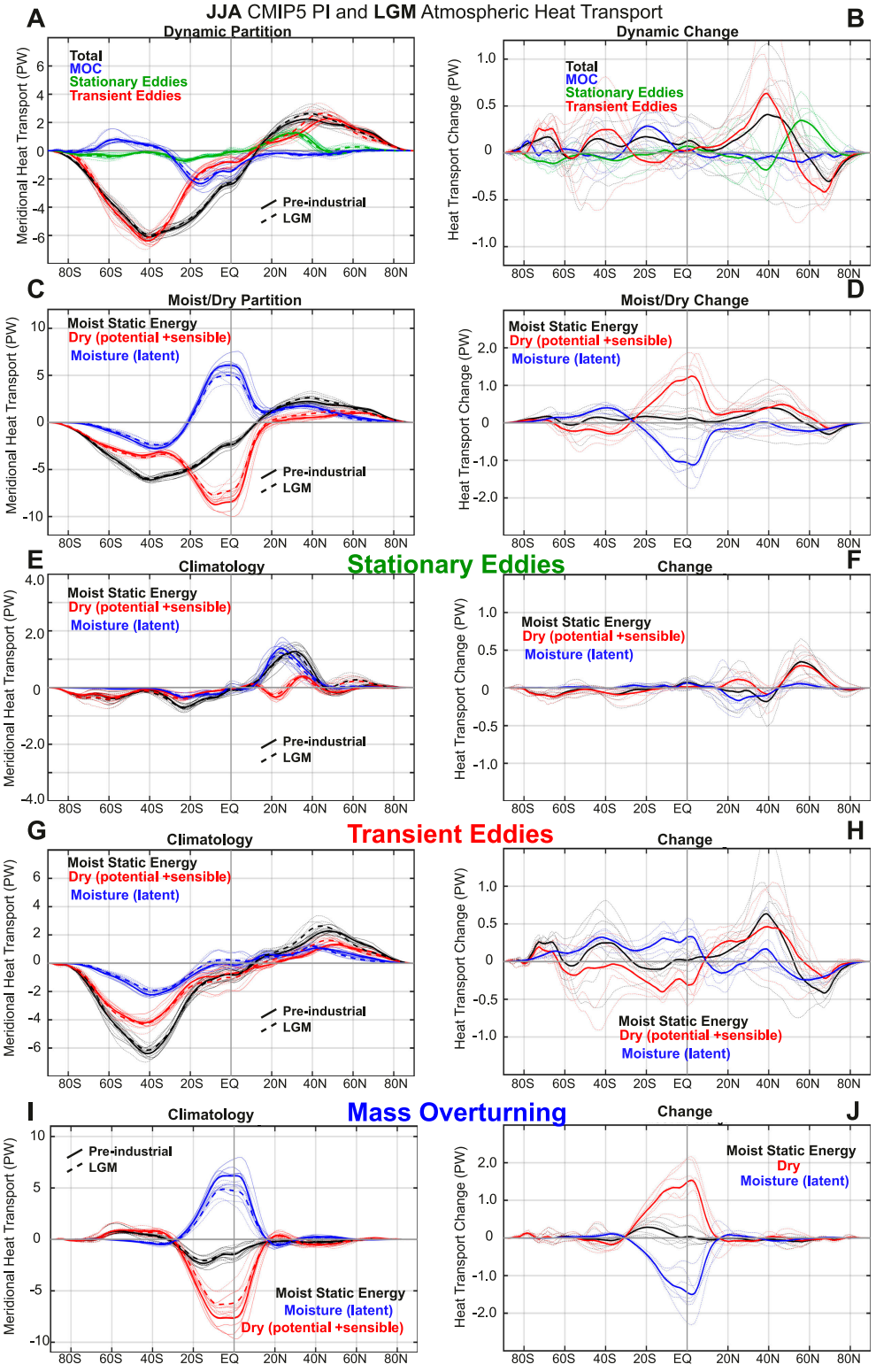

FIG. 10. As in Fig. 8, but for JJA.

energy transport under 4 × CO_2. Overall, the changes in MHT are small and spatially smooth, but the partitioning of those changes between circulations is larger in magnitude, highly variable with latitude, and differs between climate models (e.g., Figs. 5b and 8b).

Stone (1978) and Farneti and Vallis (2013) both speculated that MHT_{MAX} is insensitive to changes in climate state because the atmosphere is efficient at transporting energy. The compensating changes between energy transports in the different dynamical components (AHT, OHT, SE, TE, MOC) and between latent and sensible heat seen here are consistent with the notion of efficient atmospheric energy transport (Z. Liu et al. 2018). However, in a system with efficient dynamics, radiative forcing at the equator-to-pole scale is primarily balanced by MHT changes (Yang et al. 2016, 2015b). The lack of MHT changes under LGM forcing—which is substantial at the equator-to-pole scale (Braconnot et al. 2007b)—seems at odds with the paradigm of efficient dynamics. Additionally, radiative feedbacks have substantial structure at the equator-to-pole scale (Feldl and Roe 2013; Armour et al. 2013), which would also be expected to result in changes in MHT in the limit of efficient dynamics since the homogenization of temperature results in spatially variant radiative response. We offer a possible explanation to reconcile this apparent paradox below.

An emerging body of work has argued that, in response to external forcing, atmospheric motions move energy from regions that are inefficient at radiating energy to space to regions that are efficient at radiating energy to space (Roe et al. 2015; Feldl and Roe 2013; Frierson and Hwang 2012) by diffusing moist static energy (Armour et al. 2019)—the sum of latent and sensible energy in the atmosphere. In the MSE diffusion framework, temperature changes in the deep tropics have a larger (factor of 3) impact on AHT than equal magnitude temperature changes in the high latitudes (Liu et al. 2016) because of the exponential nature in the water vapor dependence on temperature at fixed relative humidity. This framework provides two complimentary perspectives on the near invariance of MHT in a changing climate:

- The temperature response in regions of weaker (negative) radiative feedbacks will be greater than that in regions of stronger (negative) radiative feedbacks resulting in smaller regional differences in the net radiative response (e.g., the temperature response times the feedback; Armour et al. 2019) resulting in small changes in the MHT.
- Although forcing yields temperature changes that are polar amplified (because radiative feedbacks are less negative in the high latitudes; Armour et al. 2013, 2019) changes in moisture are greater in the tropics than in the polar regions. As a result, the meridional profile of the change in MSE is relatively flat (Frierson et al. 2006) and there is little change in MHT.

The MSE diffusion framework provides an explanation for why TOA net radiation changes in response to climate forcing are substantial at local scales yet are nearly immutable at the equator-to-pole scale. For example, in the LGM simulations there is a substantial ($\approx$10 W m^{-2}) zonal-mean decrease in net radiation at the TOA over the Laurentide ice sheet (where the reduction in ASR exceeds that in OLR locally) but a nearly equal-magnitude increase in net radiation poleward of 70°N where the decrease in OLR associated with cooling is unaccompanied by compensating ASR changes (Fig. 2e) over the perennial sea ice. Even in the presence of substantial regional-scale solar forcing, adjustments in the atmospheric circulation spatially smooth the temperature response resulting in temperature and OLR changes in regions outside of the localized forcing that oppose the energetic input by the forcing. As a result, the equator-to-pole gradient in ASR and OLR (ASR* and OLR*) show large magnitude, but nearly compensating changes (i.e., the near unit slope of changes in Fig. 2f) that render the MHT nearly climate-state invariant. In more general terms, dynamics are incredibly efficient at counteracting forcing at small scales and do so by smoothing temperature outside the region of forcing. The resultant spatially averaged radiation changes are constrained by the regions of most efficient radiative damping (Pierrehumbert 1995). Thus, although dynamics may be more efficient than the *spatial-average radiative damping* of the climate system, the large-scale climate forcing is primarily balanced by radiative feedbacks in the region of most efficient radiative damping, leaving the MHT nearly unchanged.

From a dynamics perspective, the component circulations (OHT, AHT, SE, TE, MOC, moist, and dry) that make up MHT vary remarkably between models and across the ensemble of simulations analyzed here. The near invariance of total MHT is accomplished by several different compensating component changes that we list and discuss below:

- *Implied OHT versus AHT change*. In response to 4 × CO_2, the reduction in implied OHT associated with high-latitude ocean heat uptake is nearly compensated for by an increase in AHT. This near compensation is expected given that changes in OHT and ocean heat uptake modify the energy input to the atmospheric column in nearly the same way that the climatological solar insolation impacts the atmospheric column to

drive MHT: the majority of the ASR measured at the TOA is absorbed at the surface, which heats the surface and, in turn, heats the atmosphere via upward turbulent energy fluxes. In this sense, one would expect the AHT to respond to changes in implied OHT the same way it responds to a spatially localized radiative heating.

- *Moist versus dry energy transport changes*. Compensating changes in moist and dry AHT are seen in both the midlatitude TEs and the tropical Hadley cells (MOC) as the atmosphere warms and moistens (cools and dries). In both regions, the climatological moisture transport is enhanced with warming. These changes are expected from unchanged atmospheric circulations with increased moisture. The enhanced moisture content of the lower troposphere and slight increase in gross moist stability of the tropical atmosphere with warming (Chou and Chen 2010; Ma et al. 2012; Chou et al. 2013) leads to compensating changes in MOC tropical moisture import and dry static energy export in the surface and upper branches of the Hadley cell, respectively, with little net change (Hill et al. 2015). In the midlatitudes, the opposing changes in TE moist and dry transports with warming result from an enhanced midlatitude meridional gradient of moisture (which results from the nonlinear Clausius–Clapeyron equation) and reduced meridional temperature gradient (Held and Soden 2006).
- *Stationary versus transient eddy heat transport changes*. The ensemble-mean response to the Laurentide ice sheet in the LGM features an increase in SE and a decrease in TE in the NH. Additionally, although the change in SE in response to $4 \times CO_2$ differs markedly between models, for each model the change in TE opposes the change in SE. As a result, the net change in AHT is both smaller in magnitude and spatially smoother than the component changes. Donohoe and Battisti (2009) argue that the poleward deflection of the LGM jet over the Laurentide ice sheet steers storms away from the Atlantic storm track, thereby reducing the seeding of storms and the zonally averaged storminess. This result suggest that enhanced stationary wave amplitude can directly reduce the zonal-mean transient eddy strength by steering storms away from the baroclinic zone that support storm growth (Kaspi and Schneider 2013).
- *Transient eddy versus meridional overturning circulation heat transport changes*. In the midlatitudes, changes in the MOC in the Ferrel cell oppose changes in TE. Similarly, in the tropics during the solstice seasons, models have stronger TE out of the summer hemisphere than observed but weaker MOC than observed. We note that this compensation between MOC and TE is expected on theoretical grounds by the following mechanism. Vertical motion in the atmosphere is thermodynamically constrained such that the adiabatic cooling/heating balances the TE divergence/convergence minus the radiative damping to space. Thus, stronger midlatitude TE cause enhanced upwelling on the poleward flank of the storm track and, by mass continuity, an enhanced MOC in the Ferrel cell with equatorward AHT. Similarly, the midlatitude TE implicitly impacts the strength of the Hadley cell in even the most basic axially symmetric theory (Held and Hou 1980) by way of the diabatic cooling induced by TE divergence in the subtropics. The compensation between MOC and TE helps explain why changes in MHT are small and meridionally smooth because the vertical motion in the overturning circulation responds to the residual of the radiative fluxes and TE divergence. This mechanism seems to play an important role in moderating the strength of MHT in idealized models where radiation is modeled as a Newtonian cooling (Held and Suarez 1994) but we suspect plays a smaller role in an atmosphere with realistic radiative processes.

TE changes are central to all the compensating changes seen in this work and we hypothesize that the adjustment of TE is paramount to maintaining the near invariance of MHT by the following mechanism: TE responds to changes in the spatial gradients of atmospheric diabatic heating independent of what process gives rise to the heating anomaly. Therefore, a regional change in radiative forcing, implied OHT divergence, or SE divergence will lead to gradients in atmospheric heating that are efficiently smoothed out by TE. Thus, models may differ in simulating the local radiative response to forcing, the mechanical response of SEs or ocean heat uptake but these intermodel differences will be compensated by changes in TE that will act to smooth out the net radiative response. In this sense, TE render the large-scale MHT insensitive to the details of radiation and dynamics by homogenizing the net radiative changes at the equator-to-pole scale.

Acknowledgments. We thank Edward Blanchard-Wrigglesworth for running the CESM simulations with saved instantaneous eddy covariances. We also thank Isaac Held, Geoff Vallis, and two anonymous reviewers for thoughtful suggestions that helped expand and clarify the manuscript. AD's work was partially funded by the National Science Foundation Paleo Perspective on Climate Change (P2C2) Grant AGS-1702827 and the NSF Antarctic Program Grant PLR 1643436. KCA received support from National Science Foundation Award AGS-1752796. LCH received support

from the National Science Foundation Graduate Research Fellowship Program GRFP-2018266662.

Data availability statement: All data used in this work are publicly available through the World Climate Research Program (WCRP) Coupled Model Intercomparison Project 5 (CMIP5), European Centre for Medium-Range Weather Forecasts, National Centers for Environmental Prediction, and the National Aeronautics and Space Administration Langley Research Center websites. Please see citations within the data and methods section of this manuscript for more information.

APPENDIX

Methodology for Partitioning MHT, AHT, and OHT over the Seasonal Cycle

The decomposition of annual mean MHT into AHT and OHT in coupled climate models is compared to that derived from observed TOA radiation and atmospheric reanalyses in Fig. A1. We describe the additional steps that are taken to calculate the climatological seasonal cycle of the various components of energy transport, which involves taking into account the energy and moisture storage in the atmospheric column. For example, the AHT into a polar cap is balanced by the net radiative input at TOA, minus the downward SHF and the atmospheric column energy tendency ($\text{Storage}_{\text{atmos}}$):

$$\text{AHT}(\theta)_{\text{seasonal}} = -2\pi a^2 \int_{\theta}^{90} \cos(\Theta)(\text{ASR} - \text{OLR} - \text{SHF} - \text{Storage}_{\text{atmos}})\, d\Theta, \tag{A1}$$

which is derived from the combination of Eqs. (1), (3), and (4) with the addition of $\text{Storage}_{\text{atmos}}$. The atmospheric energy storage is derived from the monthly mean, three-dimensional atmospheric temperature and humidity:

$$\text{Storage}_{\text{atmos}} = \frac{1}{g}\int_0^{P_s} \frac{d}{dt}(c_p T + Lq)\, dp. \tag{A2}$$

Note that the geopotential term gZ does *not* appear in the integrand because an atmosphere in hydrostatic balance can only raise its center of gravity by thermal expansion, and this contribution is accounted by use of the heat capacity at constant pressure (Trenberth 1997). The time derivative in the integrand is calculated from the centered finite difference of temporally adjacent monthly data; the surface pressure P_s in the limit of the integral is set to annual-mean values to maintain consistency with the mass balance used in the calculation of the MOC (Liang et al. 2018).

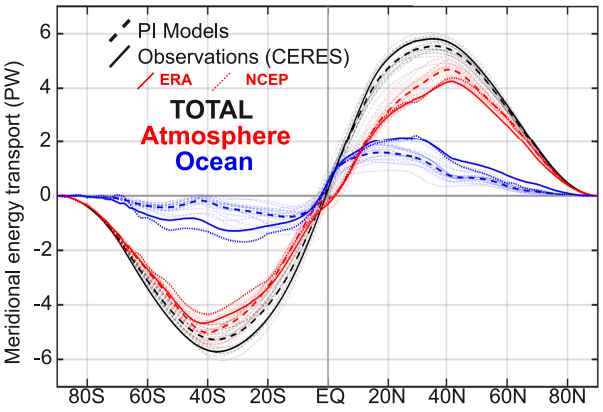

FIG. A1. Partitioning of annual-mean (black) MHT between AHT (red) and OHT (blue) in CMIP5 PI simulations and observations. The observational calculations are shown in solid lines with the MHT calculated from CERES, the AHT from the 6-hourly ERA reanalysis, and the OHT as a residual. The dotted lines show a second observational calculation of AHT derived from NCEP reanalysis and the OHT from residual of CERES-derived MHT and the NCEP AHT. The thin dashed lines show the individual CMIP5 PI simulations, and the thick dashed line shows the model ensemble average.

In principle, energy conservation demands that the globally averaged TOA radiation is equal to the sum of SHF and $\text{Storage}_{\text{atmos}}$ thus ensuring that $\text{AHT}(\theta)_{\text{seasonal}}$ in Eq. (A1) is independent of whether the integral is performed from θ to the North Pole or (the negative of that) from the South Pole to θ. In practice, we remove the global mean of each term[A1] prior to calculating the implied AHT to ensure zero transport through the poles. These global-mean corrections are of order $1\,\text{W}\,\text{m}^{-2}$ for the net diabatic heating of the atmosphere, which corresponds to an uncertainty in AHT_{MAX} of 0.2 PW.

Similar adjustments for the atmospheric moisture tendency are made in the calculation of the poleward moisture transport from $P - E$:

$$\text{AHT}(\theta)_{\text{moist, seasonal}} = -2\pi a^2 \int_{\theta}^{90} L\cos(\Theta)\left[E(\Theta) - P(\Theta) - \frac{1}{g}\int_0^{P_s}\frac{d}{dt}q(\Theta)\, dp\right] d\Theta. \tag{A3}$$

[A1] The global-mean TOA radiation and SHF are each of order $10\,\text{W}\,\text{m}^{-2}$ on seasonal time scales (Fasullo and Trenberth 2008a) due to the eccentricity of Earth's orbit about the sun, while the sum of global-mean TOA radiation, SHF, and $\text{Storage}_{\text{atmos}}$ is energetically constrained to be zero.

Additional caution must be taken when interpreting the implied OHT from the surface heat fluxes via Eq. (4) on seasonal time scales because the surface heat flux is balanced by the sum of ocean heat transport divergence and ocean heat content changes, the latter of which has magnitudes of order $300\,\mathrm{W\,m^{-2}}$ over the entire extratropics seasonally. On seasonal and interannual time scales, the surface energy budget in the extratropics is primarily a balance between SHF and the tendency in ocean heat content (Fasullo and Trenberth 2008b; Donohoe et al. 2014). Hence, the implied OHT from Eq. (4) is more aptly termed the ocean heat transport plus storage. For this reason, we will only discuss OHT in the annual mean. The seasonal cycle in OHT can be calculated by subtracting the seasonally averaged surface heat flux from the tendency of the vertically integrated ocean heat content where the latter is calculated using the three-dimensional ocean temperature output as in Donohoe et al. (2014) and Armour et al. (2016). This endeavor is beyond the scope of the current work.

The seasonal SE and MOC atmospheric energy transport (and their moist/dry partitioning) are calculated using Eq. (3) with monthly mean fields. The total AHT by the TE for each month is calculated as the residual of total AHT from Eq. (A1) and the SE and MOC contributions. The moist TE transport is calculated from the residual of the total $\mathrm{AHT}_{\mathrm{moist,seasonal}}$ using Eq. (A3) and the moist SE and MOC transports. Finally, the dry TE transport is calculated as the residual of the total TE AHT and the moist TE transport.

REFERENCES

Armour, K., C. Bitz, and G. Roe, 2013: Time-varying climate sensitivity from regional feedbacks. *J. Climate*, **26**, 4518–4534, https://doi.org/10.1175/JCLI-D-12-00544.1.

——, J. Marshall, J. Scott, A. Donohoe, and E. Newsom, 2016: Southern Ocean warming delayed by circumpolar upwelling and equatorward transport. *Nat. Geosci.*, **9**, 549–554, https://doi.org/10.1038/ngeo2731.

——, N. Siler, A. Donohoe, and G. Roe, 2019: Meridional atmospheric heat transport constrained by energetics and mediated by large-scale diffusion. *J. Climate*, **32**, 3655–3680, https://doi.org/10.1175/JCLI-D-18-0563.1.

Bjerknes, J., 1964: Atlantic air-sea interaction. *Advances in Geophysics*, Vol. 10, Academic Press, 1–82, https://doi.org/10.1016/S0065-2687(08)60005-9.

Braconnot, P., and Coauthors, 2007a: Results of PMIP2 coupled simulations of the Mid-Holocene and Last Glacial Maximum—Part 1: Experiments and large-scale features. *Climate Past*, **3**, 261–277, https://doi.org/10.5194/CP-3-261-2007.

——, and Coauthors, 2007b: Results of PMIP2 coupled simulations of the Mid-Holocene and Last Glacial Maximum—Part 2: Feedbacks with emphasis on the location of the ITCZ and mid- and high latitudes heat budget. *Climate Past*, **3**, 279–296, https://doi.org/10.5194/CP-3-279-2007.

Chengfei, H., Z. Liuand, and A. Hu, 2019: The transient response of atmospheric and oceanic heat transports to anthropogenic warming. *Nat. Climate Change*, **9**, 222–226, https://doi.org/10.1038/S41558-018-0387-3.

Chou, C., and C. Chen, 2010: Depth of convection and the weakening of tropical circulation in global warming. *J. Climate*, **23**, 3019–3030, https://doi.org/10.1175/2010JCLI3383.1.

——, T.-C. Wu, and P.-H. Tan, 2013: Changes in gross moist stability in the tropics under global warming. *Climate Dyn.*, **41**, 2481–2496, https://doi.org/10.1007/s00382-013-1703-2.

Dee, D., and Coauthors, 2011: The ERA-Interim reanalysis: Configuration and performance of the data assimilation system. *Quart. J. Roy. Meteor. Soc.*, **137**, 553–597, https://doi.org/10.1002/qj.828.

Donohoe, A., and D. Battisti, 2009: Causes of reduced North Atlantic storm activity in a CAM3 simulation of the Last Glacial Maximum. *J. Climate*, **22**, 4793–4808, https://doi.org/10.1175/2009JCLI2776.1.

——, and ——, 2011: Atmospheric and surface contributions to planetary albedo. *J. Climate*, **24**, 4402–4418, https://doi.org/10.1175/2011JCLI3946.1.

——, and ——, 2012: What determines meridional heat transport in climate models? *J. Climate*, **25**, 3832–3850, https://doi.org/10.1175/JCLI-D-11-00257.1.

——, J. Marshall, D. Ferreira, and D. McGee, 2013: The relationship between ITCZ location and cross-equatorial atmospheric heat transport: From the seasonal cycle to the Last Glacial Maximum. *J. Climate*, **26**, 3597–3618, https://doi.org/10.1175/JCLI-D-12-00467.1.

——, ——, ——, K. Armour, and D. McGee, 2014: The interannual variability of tropical precipitation and interhemispheric energy transport. *J. Climate*, **27**, 3377–3392, https://doi.org/10.1175/JCLI-D-13-00499.1.

Eady, E., 1949: Long waves and cyclone waves. *Tellus*, **1**, 33–52, https://doi.org/10.3402/tellusa.v1i3.8507.

Enderton, D., and J. Marshall, 2009: Explorations of atmosphere–ocean–ice climates on an aquaplanet and their meridional energy transports. *J. Atmos. Sci.*, **66**, 1593–1611, https://doi.org/10.1175/2008JAS2680.1.

Farneti, R., and G. Vallis, 2013: Meridional energy transport in the coupled atmosphere ocean system: Compensation and partitioning. *J. Climate*, **26**, 7151–7166, https://doi.org/10.1175/JCLI-D-12-00133.1.

Fasullo, J. T., and K. E. Trenberth, 2008a: The annual cycle of the energy budget: Part 1. Global mean and land–ocean exchanges. *J. Climate*, **21**, 2297–2312, https://doi.org/10.1175/2007JCLI1935.1.

——, and ——, 2008b: The annual cycle of the energy budget: Part 2. Meridional structures and poleward transports. *J. Climate*, **21**, 2313–2325, https://doi.org/10.1175/2007JCLI1936.1.

Feldl, N., and G. Roe, 2013: The nonlinear and nonlocal nature of climate feedbacks. *J. Climate*, **26**, 8289–8304, https://doi.org/10.1175/JCLI-D-12-00631.1.

Frierson, D. M. W., and Y.-T. Hwang, 2012: Extratropical influence on ITCZ shifts in slab ocean simulations of global warming. *J. Climate*, **25**, 720–733, https://doi.org/10.1175/JCLI-D-11-00116.1.

——, I. Held, and P. Zurita-Gotor, 2006: A gray-radiation aquaplanet moist GCM. Part I: Static stability and eddy scale. *J. Climate*, **63**, 2548–2566, https://doi.org/10.1175/JAS3753.1.

Held, I., 2001: The partitioning of the poleward energy transport between the tropical ocean and atmosphere. *J. Atmos. Sci.*, **58**, 943–948, https://doi.org/10.1175/1520-0469(2001)058<0943:TPOTPE>2.0.CO;2.

——, and A. Hou, 1980: Nonlinear axially symmetric circulations in a nearly inviscid atmosphere. *J. Atmos. Sci.*, **37**, 515–533, https://doi.org/10.1175/1520-0469(1980)037<0515:NASCIA>2.0.CO;2.

——, and M. Suarez, 1994: A proposal for the intercomparison of the dynamical cores of atmospheric general circulation models. *Bull. Amer. Meteor. Soc.*, **75**, 1825–1830, https://doi.org/10.1175/1520-0477(1994)075<1825:APFTIO>2.0.CO;2.

——, and B. Soden, 2006: Robust responses of the hydrological cycle to global warming. *J. Adv. Model. Earth Syst.*, **19**, 5686–5699, https://doi.org/10.1175/JCLI3990.1.

Hill, S., Y. Ming, and I. Held, 2015: Mechanisms of forced tropical meridional energy flux change. *J. Climate*, **28**, 1725–1742, https://doi.org/10.1175/JCLI-D-14-00165.1.

Hobbs, W., M. Palmer, and D. Monselesan, 2016: An energy conservation analysis of ocean drift in the CMIP5 global coupled models. *J. Climate*, **29**, 1639–1653, https://doi.org/10.1175/JCLI-D-15-0477.1.

Holland, M. M., and C. Bitz, 2003: Polar amplification of climate change in coupled models. *Climate Dyn.*, **21**, 221–232, https://doi.org/10.1007/s00382-003-0332-6.

Hori, M., and H. Ueda, 2006: Impact of global warming on the East Asian winter monsoon as revealed by nine coupled atmosphere-ocean GCMs. *Geophys. Res. Lett.*, **33**, L03713, https://doi.org/10.1029/2005GL024961.

Huang, Y., and M. Zhang, 2014: The implication of radiative forcing and feedback for meridional energy transport. *Geophys. Res. Lett.*, **41**, 1665–1672, https://doi.org/10.1002/2013GL059079.

Hurley, J., and W. Boos, 2015: A global climatology of monsoon low-pressure systems. *Quart. J. Roy. Meteor. Soc.*, **141**, 1049–1064, https://doi.org/10.1002/qj.2447.

Hwang, Y., and D. Frierson, 2010: Increasing atmospheric poleward energy transport with global warming. *Geophys. Res. Lett.*, **37**, L24807, https://doi.org/10.1029/2010GL045440.

——, ——, and J. Kay, 2011: Coupling between Arctic feedbacks and changes in poleward energy transport. *Geophys. Res. Lett.*, **38**, L17704, https://doi.org/10.1029/2011GL048546.

Johnson, G., J. Lyman, and N. Loeb, 2016: Improving estimates of Earth's energy imbalance. *Nat. Climate Change*, **6**, 639–640, https://doi.org/10.1038/nclimate3043.

Kalnay, E., and Coauthors, 1996: The NCEP/NCAR 40-Year Reanalysis Project. *Bull. Amer. Meteor. Soc.*, **77**, 437–471, https://doi.org/10.1175/1520-0477(1996)077<0437:TNYRP>2.0.CO;2.

Kaspi, Y., and T. Schneider, 2013: The role of stationary eddies in shaping midlatitude storm tracks. *J. Atmos. Sci.*, **70**, 2596–2613, https://doi.org/10.1175/JAS-D-12-082.1.

Li, C., and D. Battisti, 2008: Reduced Atlantic storminess during Last Glacial Maximum: Evidence from a coupled climate model. *J. Climate*, **21**, 3561–3579, https://doi.org/10.1175/2007JCLI2166.1.

Liang, M., A. Czaja, R. Graversen, and R. Tailleux, 2018: Poleward energy transport: Is the standard definition physically relevant at all time scales? *Climate Dyn.*, **50**, 1785–1797, https://doi.org/10.1007/s00382-017-3722-x.

Liu, X., D. Battisti, and A. Donohoe, 2018: Tropical precipitation and cross-equatorial ocean heat transport during the mid-Holocene. *J. Climate*, **30**, 3529–3547, https://doi.org/10.1175/JCLI-D-16-0502.1.

Liu, Z., H. Yang, C. He, and Y. Zhao, 2016: A theory for Bjerknes compensation: The role of climate feedback. *J. Climate*, **29**, 191–208, https://doi.org/10.1175/JCLI-D-15-0227.1.

——, C. He, and F. Lu, 2018: Local and remote responses of atmospheric and oceanic heat transports to climate forcing: Compensation versus collaboration. *J. Climate*, **31**, 6445–6460, https://doi.org/10.1175/JCLI-D-17-0675.1.

Loeb, N. G., B. A. Wielicki, D. R. Doelling, G. L. Smith, D. F. Keyes, S. Kato, N. Manalo-Smith, and T. Wong, 2009: Toward optimal closure of the Earth's top-of-atmosphere radiation budget. *J. Climate*, **22**, 748–766, https://doi.org/10.1175/2008JCLI2637.1.

Lorenz, E., 1953: A multiple index notation for describing atmospheric transport processes. AFCRL Rep., 35–53.

Lucarini, V., and F. Ragone, 2011: Energetics of IPCC4 AR4 climate models: Energy balance and meridional enthalpy transports. *Rev. Geophys.*, **49**, RG1001, https://doi.org/10.1029/2009RG000323.

Ma, J., S. Xie, and Y. Kosaka, 2012: Mechanisms for tropical tropospheric circulation change in response to global warming. *J. Climate*, **25**, 2979–2994, https://doi.org/10.1175/JCLI-D-11-00048.1.

Marshall, J., A. Donohoe, D. Ferreira, and D. McGee, 2014: The ocean's role in setting the mean position of the inter-tropical convergence zone. *Climate Dyn.*, **42**, 1967–1979, https://doi.org/10.1016/j.epsl.2013.12.043.

——, J. Scott, K. Armour, J. Campin, M. Kelley, and A. Romanou, 2015: The ocean's role in the transient response of climate to abrupt greenhouse gas forcing. *Climate Dyn.*, **44**, 2287–2299, https://doi.org/10.1007/s00382-014-2308-0.

Masuda, K., 1988: Meridional heat transport by the atmosphere and ocean: Analysis of FGGE data. *Tellus*, **40A**, 285–302, https://doi.org/10.1111/j.1600-0870.1988.tb00348.x.

Oort, A., 1971: The observed annual cycle in the meridional transport of atmospheric energy. *J. Atmos. Sci.*, **28**, 325–339, https://doi.org/10.1175/1520-0469(1971)028<0325:TOACIT>2.0.CO;2.

——, and T. Vonder Haar, 1976: On the observed annual cycle in the ocean–atmosphere heat balance over the Northern Hemisphere. *J. Phys. Oceanogr.*, **6**, 781–800, https://doi.org/10.1175/1520-0485(1976)006<0781:OTOACI>2.0.CO;2.

Peixoto, J., and A. Oort, 1992: *Physics of Climate.* AIP Press, 160 pp.

Pierrehumbert, R., 1995: Thermostats, radiator fins, and the local runaway greenhouse. *J. Atmos. Sci.*, **52**, 1784–1806, https://doi.org/10.1175/1520-0469(1995)052<1784:TRFATL>2.0.CO;2.

Priestley, C., 1948: Heat transport and zonal stress between latitudes. *Quart. J. Roy. Meteor. Soc.*, **75**, 28–40, https://doi.org/10.1002/qj.49707532307.

Rencurrel, M. C., and B. E. J. Rose, 2018: Exploring the climatic response to wide variations in ocean heat transport on an aquaplanet. *J. Climate*, **31**, 6299–6318, https://doi.org/10.1175/JCLI-D-17-0856.1.

——, and ——, 2020: The efficiency of the Hadley cell response to wide variations in ocean heat transport. *J. Climate*, **33**, 1643–1658, https://doi.org/10.1175/JCLI-D-19-0334.1.

Roe, G., N. Feldl, K. Armour, Y.-T. Hwang, and D. Frierson, 2015: The remote impacts of climate feedbacks on regional climate predictability. *Nat. Geosci.*, **8**, 135–139, https://doi.org/10.1038/ngeo2346.

Schneider, T., T. Bischoff, and G. Haug, 2014: Migrations and dynamics of the intertropical convergence zone. *Nature*, **513**, 45–53, https://doi.org/10.1038/nature13636.

Stone, P., 1978: Constraints on dynamical transports of energy on a spherical planet. *Dyn. Atmos. Oceans*, **2**, 123–139, https://doi.org/10.1016/0377-0265(78)90006-4.

Taylor, K., R. Stouffer, and G. Meehl, 2012: An overview of CMIP5 and the experiment design. *Bull. Amer. Meteor. Soc.*, **93**, 485–498, https://doi.org/10.1175/BAMS-D-11-00094.1.

Trenberth, K. E., 1997: Using atmospheric budgets as a constraint on surface fluxes. *J. Climate*, **10**, 2796–2809, https://doi.org/10.1175/1520-0442(1997)010<2796:UABAAC>2.0.CO;2.

——, and J. M. Caron, 2001: Estimates of meridional atmosphere and ocean heat transports. *J. Climate*, **14**, 3433–3443, https://doi.org/10.1175/1520-0442(2001)014<3433:EOMAAO>2.0.CO;2.

——, and D. P. Stepaniak, 2003a: Co-variability of components of poleward atmospheric energy transports on seasonal and interannual timescales. *J. Climate*, **16**, 3691–3705, https://doi.org/10.1175/1520-0442(2003)016<3691:COCOPA>2.0.CO;2.

——, and ——, 2003b: Seamless poleward atmospheric energy transports and implications for the Hadley circulation. *J. Climate*, **16**, 3706–3722, https://doi.org/10.1175/1520-0442(2003)016<3706:SPAETA>2.0.CO;2.

——, and ——, 2004: The flow of energy through the Earth's climate system. *Quart. J. Roy. Meteor. Soc.*, **130**, 2677–2701, https://doi.org/10.1256/qj.04.83.

——, and J. T. Fasullo, 2010: Simulation of present-day and twenty-first-century energy budgets of the southern oceans. *J. Climate*, **23**, 440–454, https://doi.org/10.1175/2009JCLI3152.1.

Vallis, G., and R. Farneti, 2009: Meridional energy transport in the coupled atmosphere ocean system: Scaling and numerical experiments. *Quart. J. Roy. Meteor. Soc.*, **135**, 1643–1660, https://doi.org/10.1002/qj.498.

Vellinga, M., and P. Wu, 2008: Relations between northward ocean and atmosphere energy transports in a coupled climate model. *J. Climate*, **21**, 561–575, https://doi.org/10.1175/2007JCLI1754.1.

Vonder Haar, T., and A. Oort, 1973: New estimate of annual poleward energy transport by Northern Hemisphere oceans. *J. Phys. Oceanogr.*, **3**, 169–172, https://doi.org/10.1175/1520-0485(1973)003<0169:NEOAPE>2.0.CO;2.

Wielicki, B., B. Barkstrom, E. Harrison, R. Lee, G. Smith, and J. Cooper, 1996: Clouds and the Earth's Radiant Energy System (CERES): An Earth observing system experiment. *Bull. Amer. Meteor. Soc.*, **77**, 853–868, https://doi.org/10.1175/1520-0477(1996)077<0853:CATERE>2.0.CO;2.

Wu, Y., M. Ting, R. Seager, H. Huang, and M. Cane, 2011: Changes in storm tracks and energy transports in a warmer climate simulated by the GFDL CM2.1 model. *Climate Dyn.*, **37**, 53–72, https://doi.org/10.1007/s00382-010-0776-4.

Xiang, Z., M. Zhao, Y. Ming, W. Yu, and S. Kang, 2018: Contrasting impacts of radiative forcing in the Southern Ocean versus southern tropics on ITCZ position and energy transport in one GFDL climate model. *J. Climate*, **31**, 5609–5628, https://doi.org/10.1175/JCLI-D-17-0566.1.

Yang, H., and H. Dai, 2015: Effect of wind forcing on the meridional heat transport in a coupled climate model: Equilibrium response. *Climate Dyn.*, **45**, 1451–1470, https://doi.org/10.1007/s00382-014-2393-0.

——, Q. Li, K. Wang, Y. Sun, and D. Sun, 2015a: Decomposing the meridional heat transport in the climate system. *Climate Dyn.*, **44**, 2751–2768, https://doi.org/10.1007/s00382-014-2380-5.

——, Y. Zhao, Q. Li, and Z. Liu, 2015b: Heat transport compensation in atmosphere and ocean over the past 22,000 years. *Nat. Sci. Rep.*, **5**, 16661, https://doi.org/10.1038/srep16661.

——, ——, and Z. Liu, 2016: Understanding Bjerknes compensation in atmosphere and ocean heat transports using a coupled box model. *J. Climate*, **29**, 2145–2160, https://doi.org/10.1175/JCLI-D-15-0281.1.

Zelinka, M., and D. Hartmann, 2012: Climate feedbacks, and their implications for poleward energy flux changes in a warming climate. *J. Climate*, **25**, 608–624, https://doi.org/10.1175/JCLI-D-11-00096.1.